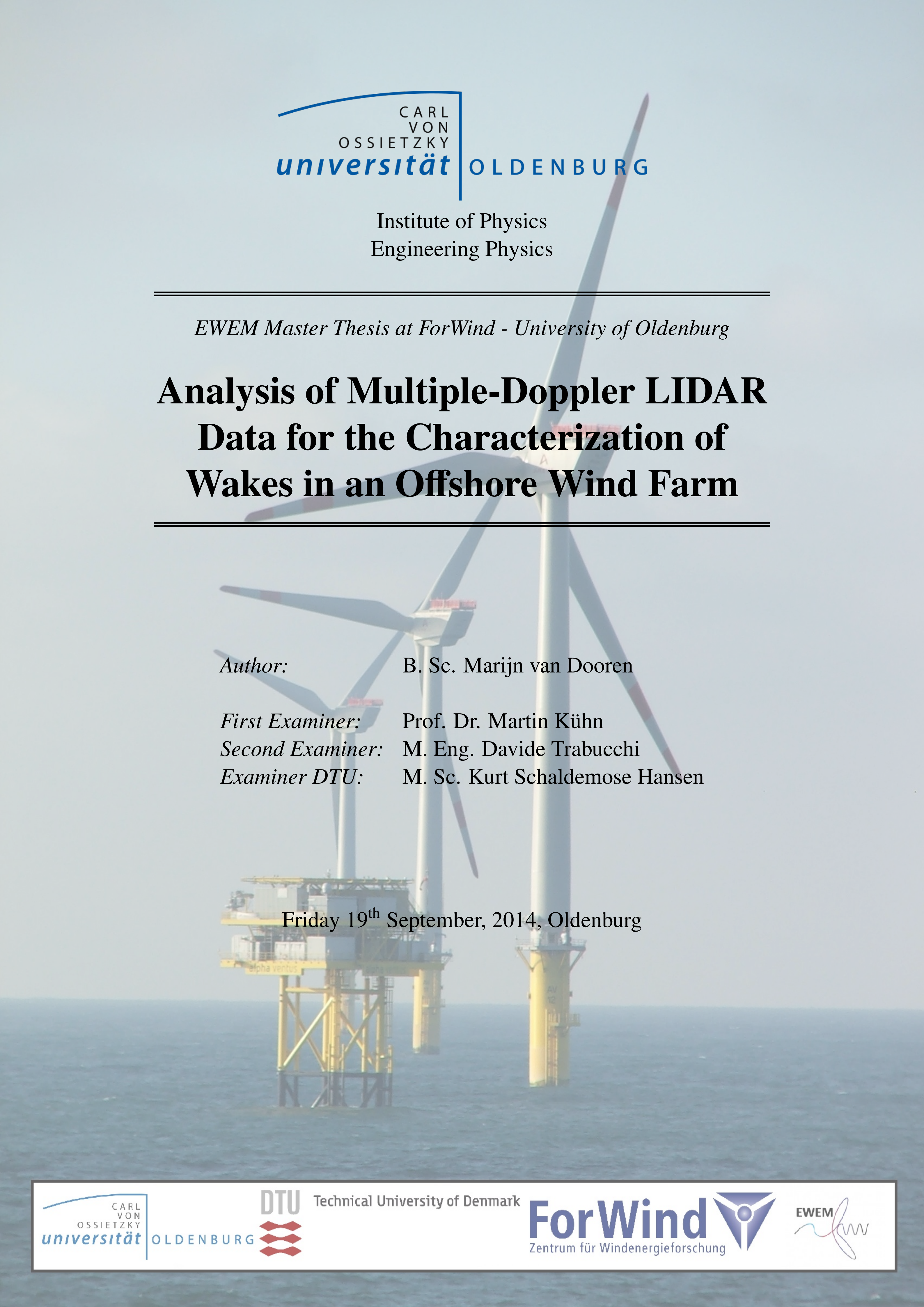

Institute of Physics
Engineering Physics

EWEM Master Thesis at ForWind - University of Oldenburg

Analysis of Multiple-Doppler LIDAR Data for the Characterization of Wakes in an Offshore Wind Farm

Author:	B. Sc. Marijn van Dooren
First Examiner:	Prof. Dr. Martin Kühn
Second Examiner:	M. Eng. Davide Trabucchi
Examiner DTU:	M. Sc. Kurt Schaldemose Hansen

Friday 19th September, 2014, Oldenburg

Technical University of Denmark

ForWind Zentrum für Windenergieforschung

Acknowledgments

I am particularly grateful for the assistance by my direct supervisor Davide Trabucchi. He dedicated a significant amount of time to discuss the scope and guide the direction of the thesis, was always readily available to answer questions and provided suggestions to improve this report.

Many thanks to my other supervisor Kurt Hansen, who clearly showed his interest in the project despite of the long-distance supervision, provided critical review from a slightly different angle and assisted on understanding and working with meteorological phenomena.

I would like to thank Martin Kühn for allowing me to write my master thesis in his group ForWind - Wind Energy Systems and supervising the project.

Many thanks to the members of the LIDAR research group at ForWind; Davide Trabucchi, Jörge Schneemann, Juan-Jose Trujillo, Hauke Beck and Stephan Voss, for the interesting discussions and the useful comments. I hope that my work provides a useful contribution to further research in the group.

I would like to express my appreciation for my full-time office colleges Atefeh, Laura, Augusto and Julian for creating a pleasant ambiance in the office which positively influenced my performance.

Last but not least, I want to thank my parents Petra van Dooren and Vincent van Dooren, and my grandfather Pierre van Dooren, for always having supported my studies financially and for motivating me to perform at my maximum level.

Contents

List of Figures

List of Tables

Nomenclature

c	Speed of light	m/s
C_h	Altitude selection parameter	-
CNR	Carrier-to-Noise Ratio	dB
C_T	Wind turbine thrust coefficient	-
D	Wind turbine rotor diameter	m
e_u	Error on the wind speed u	m/s
e_V	Error on the absolute wind speed V	m/s
e_v	Error on the wind speed v	m/s
$e_{v_{LOS}}$	Total error on v_{LOS}	m/s
e_δ	Accuracy of the measurement elevation angle	deg
$e_{\chi C}$	Accuracy of the measurement azimuth angle	deg
f_e	Emitted frequency	Hz
f_r	Reflected frequency	Hz
h	Height	m
hh	Hub height	m
i, j	Row and column index of grid	-
K	Number of measurements considered per grid point	-
K_L	Number of measurements considered per grid point per LIDAR	-
k	Single measurement point index	-
L	Monin-Obukhov length	m
MAE	Mean Absolute Error	-
n, m	Number of rows and columns of the grid	-
p	One-dimensional grid index for points	-
R	Radius of influence of circle around grid point	m
r	LIDAR scanning range	m
T_a	Air temperature	deg C
TI	Turbulence intensity	%
T_w	Water surface temperature	deg C
t	Time	s
u	Wind speed component in x-direction	m/s
V	Absolute wind speed	m/s
v	Wind speed component in y-direction	m/s
v_{LOS}	Line-of-sight velocity measured by LIDAR	m/s
W_d	Wake deficit	-
W_w	Wake width	-
w	Velocity component in z-direction	m/s
w_f	Cressman weight	-
w_L	LIDAR weight	-
x, y, z	Cartesian coordinates	m

α	Geometrical parameter	-
β	Geometrical parameter	-
γ	Relative wind direction on the nacelle	deg
$\Delta\chi$	Difference between azimuth angles of two LIDARs	deg
δ	Elevation angle	deg
$\varepsilon_{v_{LOS}}$	Accuracy of v_{LOS}	m/s
θ	Wind direction	deg
σ	Standard deviation	-
χ	Azimuth angle in the geographical reference frame	deg
χ_C	Azimuth angle in the Cartesian reference frame	deg

1 Introduction

The necessity of measuring wakes in offshore wind farms and the advantage of applying LIDAR technique will be motivated in Section 1.1. After that, the scope of the master thesis work will be clarified in the research question statement in Section 1.2. For a better understanding of the master thesis, background theory on the wake effect and LIDAR technique will be presented in Section 1.3.

1.1 Motivation

The wake effects in wind farms can decrease total power output by 10-20% [3]. On a larger scale, merged wakes of complete wind farms can affect the energy production of downstream wind farms negatively. Developing a better knowledge of wakes will enable a wind farm layout optimization for power output and an improved design of wind turbines. Since sites allocated for offshore wind farms are generally close together, the layout optimization should take into account the influence of nearby wind farms in the estimation of the annual energy yield. This makes wakes not only relevant for wind energy research, but also for the industry.

Nowadays most wake models are validated by power measurements in wind farms [21]. For the improvement of wake models, a more sophisticated method is needed, ideally the measurement of the wind speed and direction inside the wind farm wakes itself. Standard anemometry (e.g. cup or sonic anemometers) applied to measure wakes is not flexible, because these devices can only measure at one point in space. Also, the offshore installation requires considerable extra effort.

The use of LIDAR scanning technique in offshore wind farms offers several advantages. In particular:

- LIDARs are able to execute scans over a long range that can cover a large part of a wind farm in a few minutes time. In other words, they can describe the spatial evolution of single or multiple wakes. This cannot be established by one-point measurements.
- When synchronized, two or three LIDARs can enable the direct evaluation of 2D and 3D wind fields, respectively.
- Since LIDARs can be placed on existing platforms, such as wind turbine foundations and transformer platforms, there is no need to invest in additional expensive offshore support structures.

For these reasons, the application of measurements with multiple LIDARs scanning the same region in an offshore wind farm is a present-day research topic. In recent research, wakes of wind turbines have been characterized by means of both RADAR [14] and LIDAR [15]. In both of these cases, land based wind turbines were investigated. The research was based on algorithms able to calculate a multi-dimensional wind field from the radial measurements provided by the applied instruments. The measurement setup was carefully optimized according to the requirements of the algorithms used. Because the location of LIDARs in an offshore wind farm usually cannot be chosen freely, the measurement setup is not optimized for the application of any algorithms.

1.2 Research Question Statement

In this master thesis, a LIDAR measurement data processing algorithm will be developed that is able to produce a steady, 10-minute average, 2D wind field from data supplied by multiple LIDARs scanning the same region of an offshore wind farm. The main goal is to characterize wind turbine wakes within the wind farm.

Existing Multiple-Doppler LIDAR data processing algorithms will be studied and adjusted in order to be applied under the mentioned prevailing sub-optimal conditions of an offshore environment. A vital part of the research is to indicate the circumstances under which the developed algorithm can or cannot be applied with sufficient accuracy of the resulting wind field.

The algorithm will be applied to the measurements taken by the Multiple-Doppler LIDAR system installed by ForWind - University of Oldenburg in the »alpha ventus« wind farm in order to describe steady wakes inside the wind farm. From 2D wind fields evaluated by the algorithm, horizontal wake profiles will be extracted at multiple distances downstream of the wind turbine. The wake profiles will eventually be compared to a wake model generated by the program FLaP [19], which is based on the steady Ainslie wake model [2].

1.3 Background Theory on Wakes and LIDAR

To have a better understanding of the master thesis work and the issues involved, basic knowledge about the subject is required. Therefore, this chapter provides explanations on both wind turbine wake theory and LIDAR scanning technique. For more details, it is advised to read [7] and [24], respectively.

1.3.1 Wake Theory

Wind turbines are used to generate electricity by extracting energy from the wind. This means that the wind downstream of an operational turbine must have less energy than the wind upstream of the same turbine [12]. Since the energy extracted is kinetic energy, the velocity of the wind is decreased after passing through the turbine. As the wake moves away from the wind turbine, it expands, mixes with the ambient flow and recovers. Especially when constructing a wind farm, it is important to know how large the velocity deficit in a wake is and how long it takes before the wake recovers. Wakes can still be present at a distance of 10-15 wind turbine diameters downstream of a turbine. The shape and behavior of a wake is highly dependent on:

- The ambient turbulence

- The atmospheric stratification and vertical velocity profile
- Wind turbine thrust coefficient
- Wind turbine yaw misalignment

Multiple different engineering wake models exist, with varying complexity and accuracy. Most of these models rely on empirical approaches to calculate the velocity deficit of the near wake, the wake width development and the effects on the turbulence intensity. Some of these models include fluid dynamics considerations. These engineering wake models are interesting, because they have lower computational needs than a full CFD simulation of a wake. Three examples are given here:

- Jensen [16] - This model assumes a linear wake expansion and approximates the velocity deficit as a function of distance downstream of the turbine. The velocity deficit is assumed to be constant within the wake width and therefore a discontinuity is found at precisely the wake width. Because the simplicity and linearity of this model, it can be used to model wake effects of a complete wind farm by using superposition of the velocity profiles for single turbines.
- Frandsen [11] - This model uses an exponential function to approximate the wake width as a function of downstream distance and then estimates the velocity deficit. Like the Jensen model, the velocity deficit is assumed to be constant within the wake width and a discontinuity occurs. The method is specifically developed to model the multiple wake of a wind farm.
- Ainslie [2] - This model combines empirical estimations of the wake width and center line velocity deficit with a simplified Navier-Stokes equation and the continuity equation from fluid dynamics [18]. Initially a Gaussian velocity deficit profile at a distance of 2 turbine diameters downstream is assumed, with a linear wake expansion and wind speed recovery. Then, the fluid dynamics equations are iteratively solved to calculate a 2D wake wind field. The model will converge in approximately 5 to 10 iterations.

1.3.2 Doppler LIDAR Scanning Technique

The abbreviation LIDAR stands for 'light detection and ranging'. With this remote sensing technique, aerosols (tiny particles) in the air are used to reflect an emitted laser beam [24]. These particles are assumed to have the same velocity as the wind itself. A schematic view of this principle can be observed in Figure 1.1.

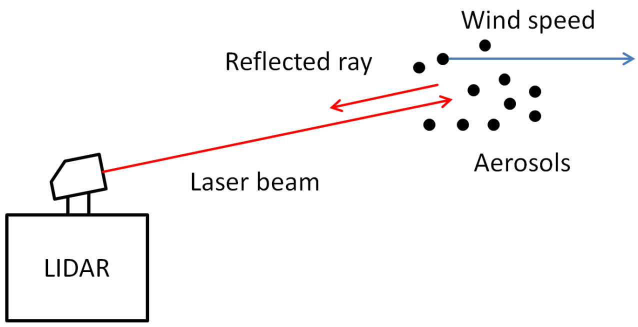

Figure 1.1: *Schematic view of the basic LIDAR principle.*

The speed of these particles, thus the wind speed, causes the frequency of the laser light to change according to the Doppler effect:

$$f_r = f_e\left(1 + 2\frac{v_{LOS}}{c}\right) \tag{1.1}$$

Note that the Doppler shift only applies to the line-of-sight wind speed component v_{LOS}. In the formula, f_e and f_r are the emitted and reflected light frequencies, respectively and c is the speed of light. Because light frequencies are high (infra-red has frequencies in the range of 10^{12} Hz) and the wind speed is relatively low compared to the speed of light, the frequency shift is hard to determine if the two signals are evaluated separately. For this reason, the difference of the emitted and reflected signal is computed. The resulting signal then has a frequency proportional to the Doppler frequency shift. This phenomenon is called the ‘beat’ frequency (see Figure 1.2). A Fast Fourier Transform (FFT) can be applied on this signal in order to determine the frequency shift and thus the wind speed.

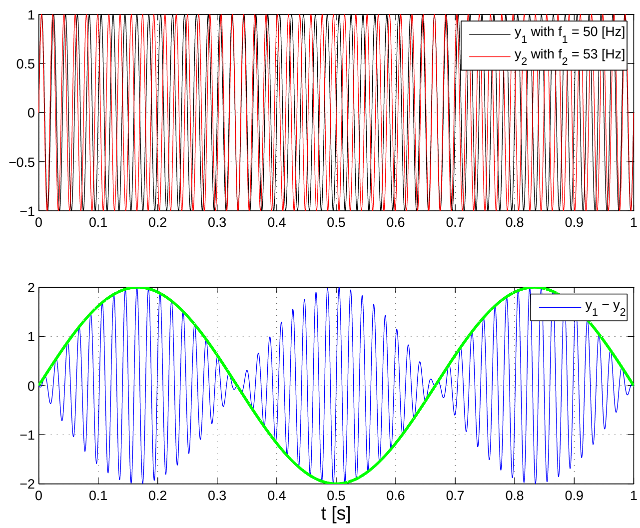

Figure 1.2: *Determination of frequency shift with the beat effect.*

In Figure 1.2, two arbitrary signals with frequencies 50 and 53 Hz are shown. The difference of these two signals is plotted and a new signal (green curve) with a frequency of 1.5 Hz, half of the difference, can be seen.

Note that on average, for each 10^6 photons emitted by the laser, only 1 is reflected back. Since the noise level is high, it is not sufficient to calculate the frequency shift by the FFT of just one sample. Therefore, the FFT is evaluated for hundreds of samples and the resulting spectra are averaged. In this way, the Doppler peak which characterizes all samples can be identified easily.

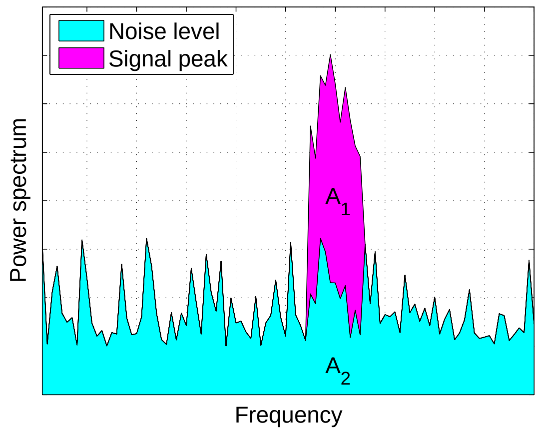

Figure 1.3: *Averaged frequency spectrum example.*

Figure 1.3 illustrates an example of an averaged frequency spectrum, with the signal peak and the noise level defined by colored areas. Randomly generated data was used to make this plot. To assess the quality of a measurement, the Carrier-to-Noise Ratio CNR is defined with Equation 1.2 [23]. It is measured in the unit dB. This signal will be used as a selection criterion for measurement data further on in the report.

$$CNR = 20\log_{10}\left(\frac{A_1}{A_2}\right) \tag{1.2}$$

There are two main categories of LIDAR scanners:

1. Continuous wave LIDARs: A continuous signal is emitted and reflected mainly around the focus point. Although aerosols located at any point on the line-of-sight will reflect part of the signal, the contributions of the distances far away from the focus point are insignificant.

2. Pulsed LIDARs: Laser pulses with time lengths in the order of hundreds of ns are emitted. Since the signal is not reflected at a uniquely determined distance but over the whole line-of-sight, the pulses appear elongated when received back. The return signal can be cut into time domains, of which the time of flight can be calculated. Because the speed of light is a constant, these time domains directly correspond to different ranges, i.e. locations of reflection. For each pulse, the v_{LOS} can therefore be estimated at multiple ranges on the line-of-sight.

Most LIDARs point the laser beam with a top piece that can be rotated around two axes or an internal rotating mirror. The direction of the laser beam can be described by two angles; the azimuth angle χ and the elevation angle δ. The azimuth angle is either measured clockwise positive from the north (geographical reference frame) or anti-clockwise positive from the x-axis (Cartesian reference frame). They are referred to as χ and χ_C, respectively. See the relation between these two angles in Equation 1.3. The azimuth is measured in a horizontal plane. The elevation is the angle measured upwards from the horizontal plane.

$$\chi_C = \frac{\pi}{2} - \chi \tag{1.3}$$

The basic remote sensing principle for LIDAR is that it evaluates the line-of-sight velocity v_{LOS}, which is actually a one-dimensional projection of the real wind vector V. In Figure 1.4, a 2D plane is shown with one LIDAR measurement taking place. The line-of-sight velocity measurement, the total wind vector and the components u and v are indicated. The direction of the wind vector is θ. On the right, the LIDAR formula is shown.

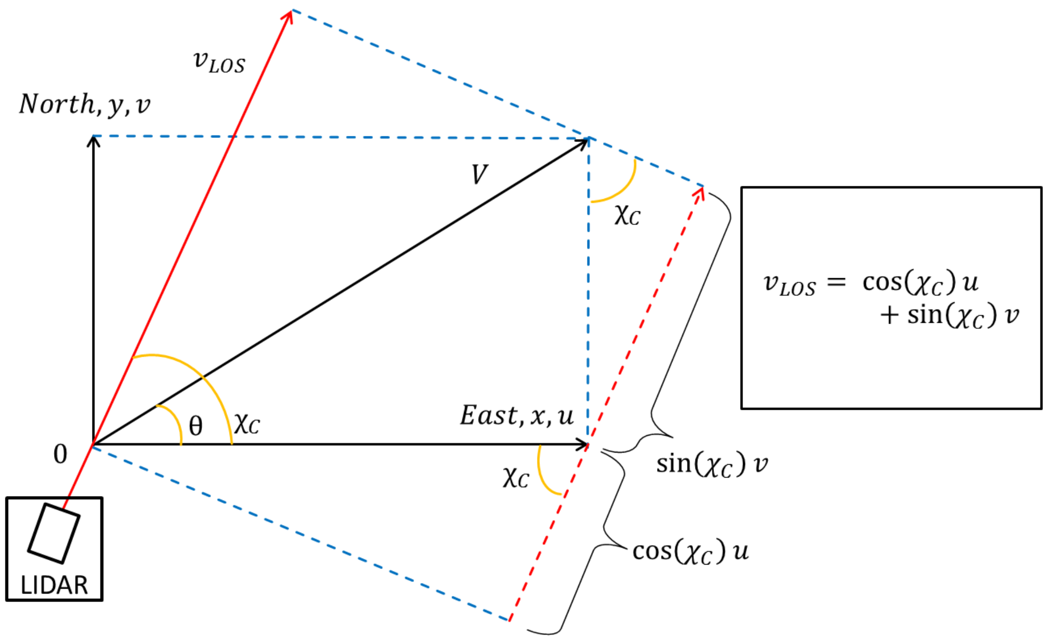

Figure 1.4: *Top view of the geometry of a LIDAR measurement.*

For a 3D wind vector evaluation, three measurements are needed. The elevation δ is introduced and the LIDAR formula reported in Figure 1.4 changes to:

$$v_{LOS} = \cos(\chi_C)\cos(\delta)u + \sin(\chi_C)\cos(\delta)v + \sin(\delta)w \tag{1.4}$$

The velocity components u, v and w can be evaluated with multiple v_{LOS} measurements of either one LIDAR or multiple LIDARs. The way in which this is done, depends on the purpose of the measurement. Different LIDAR types exist to accommodate different scanning methods. An overview of common scanning methods is stated here:

- PPI (Plan Position Indicator) - This scan has a fixed elevation angle and a varying azimuth angle. This is often used by pulsed LIDARs with a very low elevation to make a horizontal plane scan.

- RHI (Range Height Indicator) - This scan has a fixed azimuth angle and a varying elevation angle. This type of scan can be used for establishing a vertical wind profile.

- VAD (Vertical Azimuth Display) - This scanning method is actually based on a PPI with a high elevation (mostly $\delta = 60°$). A continuous LIDAR is generally used for this scan. It takes v_{LOS} measurement along a circle in a horizontal plane and fits a squared sine curve through the measurements. The wind speed and direction can be derived from the sinusoid. The time resolution is generally 1 second. Because this scan combines measurements taken at different locations at different moments in time, the wind field is assumed to be homogeneous and steady.

- DBS (Doppler Beam Swing) - Similar to the VAD, but it only takes four measurements at the cardinal positions (north, east, south, west). Again, a homogeneous and steady wind field has to be assumed. A DBS is normally executed with a pulsed LIDAR, such that a 3D wind vector can be established simultaneously at multiple altitudes.

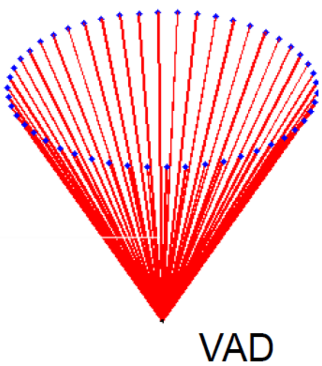

Figure 1.5: *Schematic view of a VAD scan [23].*

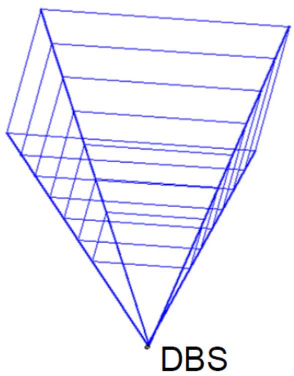

Figure 1.6: *Schematic view of a DBS scan [23].*

2 Multiple-LIDAR Wind Field Evaluation Algorithm

This chapter describes the development, verification and validation of the Multiple-LIDAR Wind Field Evaluation Algorithm, abbreviated as MuLiWEA. The development consists of three parts:

- Section 2.1 will describe the methodology of the MuLiWEA.
- Section 2.2 contains the estimation of the measurement errors on the LIDAR system and the numerical errors associated with the MuLiWEA processing. This way, the LIDAR data and the MuLiWEA can be verified.
- Section 2.3 clarifies how MuLiWEA is validated by applying the algorithm on simulated LIDAR measurements made in a simulated wind field and then comparing the evaluated wind field to the simulated one.

2.1 Methodology

Different existing algorithms were studied to establish a best way to process the Multiple-Doppler LIDAR data in order to characterize wake effects. Simplifications and adjustments were imposed on the algorithms to be able to apply MuLiWEA on the available measurement data with the limitations mentioned in Chapter 1. The most important algorithms considered for establishing the MuLiWEA are 2D versions of the algorithm as explained by Chong [8] as the Quad-Doppler wind synthesis and the Multiple-Doppler Synthesis and Continuity Adjustment Technique (MUSCAT) by Bousquet [5], [6], [10]. These techniques are developed to be applied on airborne RADAR measurements for meso-scale atmospheric wind analysis. For the application on wakes in wind farms, the methodology will be adjusted accordingly.

The basic scope of any Multiple-Doppler algorithm is to generate a local wind speed vector $[u\ v\ w]$ based on the line-of-sight speed v_{LOS} measured along different directions in a well defined control volume by different LIDARs. In the scope of this master thesis, the vertical wind speed w is assumed to be zero. This means that a 2D wind vector $[u\ v]$ will be generated. The approach is based on a geometrical wind vector evaluation, but has a adjustment imposed by the continuity equation.

2.1.1 Underlying Assumptions of MuLiWEA

It is important to note that several assumptions had to be made in order to establish the algorithm and apply it to this specific research. They are listed and explained below:

1. The vertical speed w is neglected. This is a reasonable solution to a practical issue; the elevation angles with which the LIDARs measure, are too low to be able to retrieve a vertical wind speed component larger than the noise level.

The validity of this assumption is expected from neutral atmospheric stratification. Its application outside from this condition should be treated with care.

2. It is assumed that the continuity equation can be applied in the horizontal plane. It means that there is no transport of momentum in the z-direction. This assumption is actually a direct consequence of the previously mentioned one.

3. For the continuity equation, density fluctuations are neglected. Because of the low wind speeds, incompressible flow is a valid assumption. However, density changes could be caused by the varying humidity of the air above a sea surface. These effects cannot be measured and are considered insignificant to the research.

4. The MUSCAT [6] algorithm implements a filter function which smooths large spatial variations in the wind fields. Namely, the MUSCAT is applied to meso-scale wind fields, where the mentioned variations are not expected. When a wind field contains wakes, these variations do occur and therefore the filtering feature has not been implemented in MuLiWEA.

Applying these assumptions, it is possible to evaluate the horizontal wind vector on a regular grid which covers the region where the PPI scans measured by two or more LIDARs overlap within a restricted altitude interval.

2.1.2 Geometrical Wind Vector Evaluation

According to the first assumption made in the previous subsection, the LIDAR equation can be simplified to the following for any measured point k in space:

$$\sin(\chi)\cos(\delta)u + \cos(\chi)\cos(\delta)v = v_{LOS} \tag{2.1}$$

This equation considers the azimuth (χ) and elevation (δ) angles of a LIDAR, to express the measured line-of-sight speed (v_{LOS}) in the horizontal speed components u and v. Note that the azimuth angle is expressed in the geographical reference system. Theoretically, one measurement from each of two different LIDARs - measuring with different azimuth angles - per grid point p would create a linear set of equations that could solve for the 2D wind vector. In practice, this is not applicable to overlapping PPI scans: Because of the nature of this scanning strategy, the measurements of the two considered LIDARs cannot be synchronized in time and space at the grid points p. Therefore, a specific way of interpolation will be a vital part of the algorithm. To decrease the error, multiple measurements will be considered to get an estimate for the wind speed vector at a grid point p. With this in mind, the algorithm finds its essentials in the Quad-Doppler wind synthesis by Chong [8].

The sequential steps of evaluating the wind vector is explained below:

- Sets with 10 minutes of measurement data of two overlapping PPI LIDAR scans are considered. A Cartesian grid is generated on the area where the scans overlap. In other words, data sets are selected according to a specific time *and* space domain. For convenience, the grid has two ways of indexing. Consider the grid size m-by-n. Points are indicated by the indexes (i, j). For numerical computations explained later, it is vital to define a one-dimensional index $p = i + (j-1)m$ which counts the grid points from 1 till mn. Figure 2.1 illustrates the two ways of grid indexing.

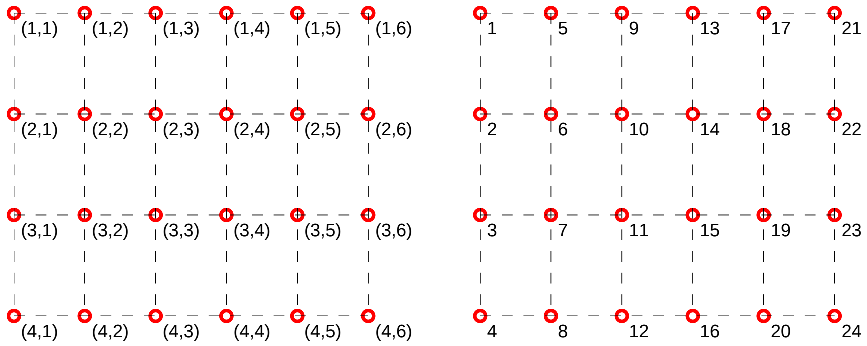

Figure 2.1: *Indexing of the grid with index i, j (left) and index p (right) for m* = 4, *n* = 6.

- Around each grid point p, a circle with radius of influence R is drawn. Each measurement point k within this circle - regardless from which LIDAR - is taken into account in the calculation of the wind speed vector at that grid point. The number of measurements taken into account at grid point p is called K. Figure 2.2 shows a Cartesian grid with an arbitrary grid point p and a red circle with radius of influence R drawn around it. For an illustrative purpose, six measurements from each of two LIDARs are contained within the circle in this figure. Measurements outside of this circle are not visualized.

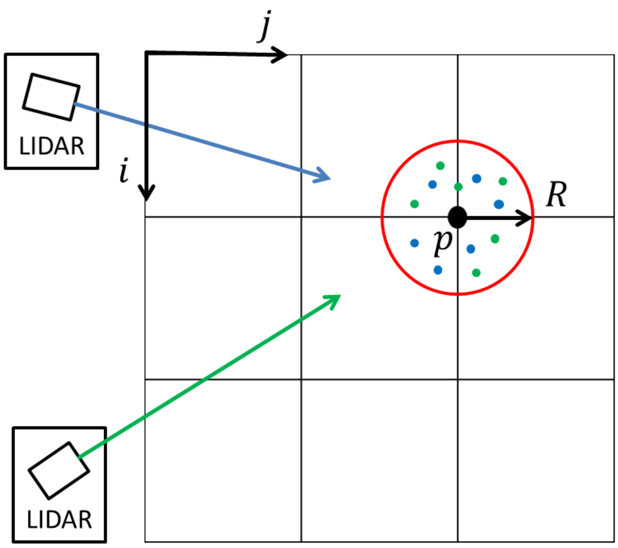

Figure 2.2: *Schematic view of a Cartesian grid and the LIDAR measurement selection around grid point p.*

- For convenience, the geometrical parameters α and β are defined:

$$\begin{aligned} \alpha &= \sin(\chi)\cos(\delta) \\ \beta &= \cos(\chi)\cos(\delta) \end{aligned} \tag{2.2}$$

  This way, Equation 2.1 can be written in a shorter form:

$$\alpha u + \beta v = v_{LOS} \tag{2.3}$$

- A linear system is established for each grid point p, which takes into account all measurements K within the circle with radius R. See Equation 2.4:

$$\begin{bmatrix} \sum_{k=1}^{K}(\alpha_k^2 w_k) & \sum_{k=1}^{K}(\alpha_k\beta_k w_k) \\ \sum_{k=1}^{K}(\alpha_k\beta_k w_k) & \sum_{k=1}^{K}(\beta_k^2 w_k) \end{bmatrix}_p \begin{bmatrix} u \\ v \end{bmatrix}_p = \begin{bmatrix} \sum_{k=1}^{K}(\alpha_k w_k v_{LOS_k}) \\ \sum_{k=1}^{K}(\beta_k w_k v_{LOS_k}) \end{bmatrix}_p \tag{2.4}$$

  The matrix equation basically consists of two lines, which are both a weighed sum of Equation 2.3: The first line is made by multiplying all terms with α, then summing over the measurement points. The second line follows the same logic, but with β as factor. As can be seen, each measurement is also weighed with the parameter w, which is the product of the two weighing functions w_f and w_L. The factor w_f is the Cressman function, which assigns a weight based on distance from the grid point. The factor w_L is a weight on the LIDAR, which makes sure that contributions from multiple LIDARs are the same, regardless of a possible difference in number of measurements available per LIDAR in the circle of influence around the grid point p. An elaborate explanation of the two weighting functions can be found in Appendix A.

- A crucial step for the benefit of the numerical computation time is the creation of a large matrix which evaluates the wind vector at all grid points simultaneously. The grid size is m-by-n, such that the total amount of points p is mn. The numbering of points p on the grid is explained in Figure 2.1. Instead of writing the 2-by-2 matrix equation for each point p, it is possible to make a sparse $2mn$-by-$2mn$ matrix M. The wind speed column vector U is now defined, which contains all mn entries for u and sub-sequentially the same amount of entries for v. The four entries of the matrix in Equation 2.4 will each be a diagonal with length mn on the sparse matrix M. A vector Q with length $2mn$ is defined, containing the terms from the vector on the right side of the equal sign in Equation 2.4.

The new linear equation can be written as:

$$M \cdot U = Q \tag{2.5}$$

With:

$$U = \begin{bmatrix} u_1 \\ \vdots \\ \vdots \\ u_{mn} \\ v_1 \\ \vdots \\ \vdots \\ v_{mn} \end{bmatrix}, \quad Q = \begin{bmatrix} \sum_{k=1}^{K} (\alpha_k w_k v_{LOS_k})_1 \\ \vdots \\ \vdots \\ \sum_{k=1}^{K} (\alpha_k w_k v_{LOS_k})_{mn} \\ \sum_{k=1}^{K} (\beta_k w_k v_{LOS_k})_1 \\ \vdots \\ \vdots \\ \sum_{k=1}^{K} (\beta_k w_k v_{LOS_k})_{mn} \end{bmatrix} \tag{2.6}$$

The sparsity structure of matrix M is shown by Figure 2.3. It can be seen that this matrix contains one sub-diagonal in each of the four quadrants. Each of these sub-diagonals represents one of the four values inside the matrix in Equation 2.4 for all grid points p.

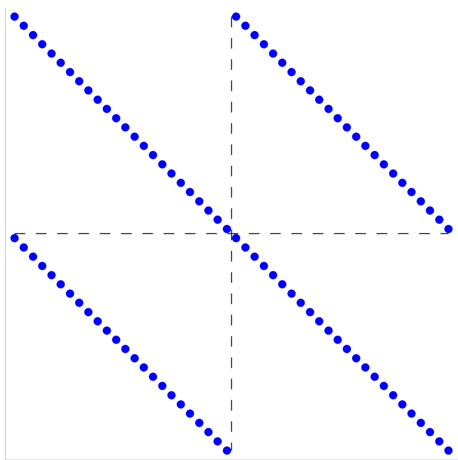

Figure 2.3: *Sparsity structure of matrix M for a grid with m* = 4, *n* = 6.

2.1.3 Continuity Equation Implementation

The idea of using a constraint for continuity and the way of implementation are extracted from the MUSCAT [6]. The continuity equation expresses the principle of the conservation of mass. When considering an infinitesimal volume of air, it has to be established that the mass that flows into this volume is equal to the mass that flows out. With neglecting variations in air density and the vertical speed, the 2D continuity equation in differential form can be written as [18]:

$$\frac{\partial u}{\partial x} + \frac{\partial v}{\partial y} = 0 \tag{2.7}$$

A numerical approximation for these derivatives can be applied on the domain of points p and included to the matrix system. The central difference scheme is used where applicable. That is, only on the boundaries of the grid there is a point missing, such that either upward or downward schemes are used. The numerical approximations for the derivatives are displayed in Table 2.1. The index (i, j) corresponds to the position on the Cartesian grid as indicated by Figure 2.2.

Derivative	Upward	Central	Downward
$\frac{\partial u}{\partial x}$	$\frac{u_{i,j+1} - u_{i,j}}{\Delta x}$	$\frac{u_{i,j+1} - u_{i,j-1}}{2\Delta x}$	$\frac{u_{i,j} - u_{i,j-1}}{\Delta x}$
$\frac{\partial v}{\partial y}$	$\frac{v_{i-1,j} - v_{i,j}}{\Delta y}$	$\frac{v_{i-1,j} - v_{i+1,j}}{2\Delta y}$	$\frac{v_{i,j} - v_{i+1,j}}{\Delta y}$

Table 2.1: *Numerical approximations for the derivatives.*

The numerical approximation of the continuity equation in this form can be added to the linear system established so far. It is chosen to add the set of linear equations to the system, which results in an *over-determined* linear system. This will make the linear system more robust. The motivation for this structure is that the basic system is sensitive to scarce amounts of data in the region of interest, the uncertainty of the measurements and the azimuth angle difference in the line-of-sight of the points k in the control volume.

By adding a part representing the continuity equation to matrix M, a new matrix M_C is generated with size $3mn$-by-$2mn$. The amount of unknown variables remains $2mn$, leaving the vector U unchanged. The vector Q_C is established by adding an amount of mn zeros to vector Q. The new linear equation is illustrated by Equation 2.8:

$$M_C \cdot U = Q_C \tag{2.8}$$

Solving this system with MATLAB, it performs a minimization of the squared error on the solution. The sparsity pattern of the matrix M_C in the final linear system is depicted in Figure 2.4. The pattern of the part of the matrix that corresponds to the continuity adjustment is a consequence of the used numerical differential schemes and the boundary conditions, combined with the specific grid indexing.

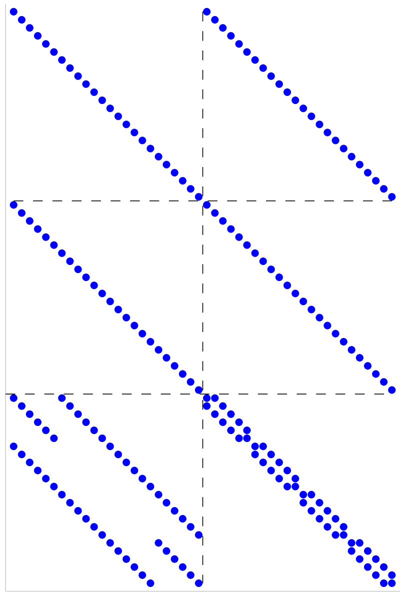

Figure 2.4: *Sparsity structure of matrix M_C for a grid with $m = 4$, $n = 6$.*

2.2 Error Analysis

In this chapter, the error on LIDAR measurements and the propagated numerical error that is imposed by the algorithm will be evaluated. The three basic accuracies of the specific LIDAR system are needed:

1. The accuracy on the measured line-of-sight component of the wind speed, $\varepsilon_{v_{LOS}}$.
2. The pointing accuracy for elevation angle, e_δ.
3. The pointing accuracy for azimuth angle, e_{χ_C}.

The goal of the analysis is to estimate the maximum error on the absolute evaluated wind speed V. It is done in three steps:

1. First the total maximum expected error on the line-of-sight velocity ($e_{v_{LOS}}$) has to be estimated. This is a function of the accuracy ($\varepsilon_{v_{LOS}}$) and also includes the influence of the azimuth and elevation accuracy.
2. After that, it is calculated how the line-of-sight velocity error ($e_{v_{LOS}}$) propagates in the numerical scheme that determines the wind speed components u and v. The numerical error propagation is calculated according to the JCGM standard [1].
3. Finally, the error on the absolute wind speed V can be determined.

2.2.1 Total Measurement Error

Note that a measured value of v_{LOS} is a projection of the real wind speed. The total error in this measurement is not only composed of the accuracy $\varepsilon_{v_{LOS}}$, but also depends on the uncertainty in the δ and χ angles. That is, there is an uncertainty in the velocity itself and also in the precise wind vector projection. Consider v_{LOS} as a projection of V and see Figure 2.5:

$$v_{LOS} = |\cos(\theta - \chi_C)\cos(\delta)V| \tag{2.9}$$

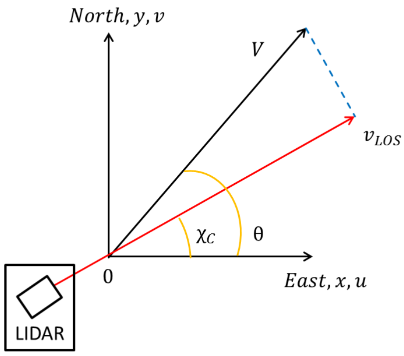

Figure 2.5: *Measuring v_{LOS} as a projection of V, top view.*

Note that in this chapter the azimuth angle in the Cartesian frame (χ_C) is used, rather than the one in the geographical frame (χ). These are explained in Section 1.3.

Two partial derivatives can be calculated to be used in the formula for the total measurement error [1]:

$$e_{v_{LOS}} = \sqrt{\varepsilon^2_{v_{LOS}} + \left(\frac{\partial v_{LOS}}{\partial \chi_C} e_{\chi_C}\right)^2 + \left(\frac{\partial v_{LOS}}{\partial \delta} e_{\delta}\right)^2} \tag{2.10}$$

2.2.2 Numerical Error

Because of the specific way of interpolation of measurement data used and the inclusion of the correction for continuity, a numerical error propagation of the MuLi-WEA cannot be done in a straight-forward manner. Therefore a simplified method is used in order to do the evaluation.

It is assumed that only one measurement from each of two LIDARs is used to evaluate the wind vector at a specific grid point. Two unknowns (u and v) can be expressed with two linear equations by the simple matrix system:

$$\begin{bmatrix} \cos(\chi_{C_1})\cos(\delta_1) & \sin(\chi_{C_1})\cos(\delta_1) \\ \cos(\chi_{C_2})\cos(\delta_2) & \sin(\chi_{C_2})\cos(\delta_2) \end{bmatrix} \begin{bmatrix} u \\ v \end{bmatrix} = \begin{bmatrix} v_{LOS_1} \\ v_{LOS_2} \end{bmatrix} \tag{2.11}$$

This is based on the LIDAR formula (see Section 1.3) for two different measurements. From the matrix equation, the wind speeds u and v can be evaluated directly:

$$u = \frac{\cos(\chi_{C_1})\cos(\delta_1)v_{LOS_2} - \cos(\chi_{C_2})\cos(\delta_2)v_{LOS_1}}{\cos(\chi_{C_1})\cos(\delta_1)\sin(\chi_{C_2})\cos(\delta_2) - \sin(\chi_{C_1})\cos(\delta_1)\cos(\chi_{C_2})\cos(\delta_2)} \tag{2.12}$$

$$v = \frac{\sin(\chi_{C_1})\cos(\delta_1)v_{LOS_2} - \sin(\chi_{C_2})\cos(\delta_2)v_{LOS_1}}{\sin(\chi_{C_1})\cos(\delta_1)\cos(\chi_{C_2})\cos(\delta_2) - \cos(\chi_{C_1})\cos(\delta_1)\sin(\chi_{C_2})\cos(\delta_2)} \tag{2.13}$$

Now it is necessary to derive a numerical error on u and v, which will be regarded to as e_u and e_v. They are both functions of all the errors associated with measured variables, i.e. the measured line-of-sight velocities and the azimuth and elevation, according to the JCGM standard for uncertainty calculations [1].

$$[e_u, e_v] = f(e_{v_{LOS_1}}, e_{v_{LOS_2}}, e_{\chi_{C_1}}, e_{\chi_{C_2}}, e_{\delta_1}, e_{\delta_2}) \tag{2.14}$$

$$e_u = \sqrt{\left(\frac{\partial u}{\partial v_{LOS_1}} e_{v_{LOS_1}}\right)^2 + \left(\frac{\partial u}{\partial v_{LOS_2}} e_{v_{LOS_2}}\right)^2 + \left(\frac{\partial u}{\partial \chi_{C_1}} e_{\chi_{C_1}}\right)^2 + \left(\frac{\partial u}{\partial \chi_{C_2}} e_{\chi_{C_2}}\right)^2 + \left(\frac{\partial u}{\partial \delta_1} e_{\delta_1}\right)^2 + \left(\frac{\partial u}{\partial \delta_2} e_{\delta_2}\right)^2} \tag{2.15}$$

$$e_v = \sqrt{\left(\frac{\partial v}{\partial v_{LOS_1}} e_{v_{LOS_1}}\right)^2 + \left(\frac{\partial v}{\partial v_{LOS_2}} e_{v_{LOS_2}}\right)^2 + \left(\frac{\partial v}{\partial \chi_{C_1}} e_{\chi_{C_1}}\right)^2 + \left(\frac{\partial v}{\partial \chi_{C_2}} e_{\chi_{C_2}}\right)^2 + \left(\frac{\partial v}{\partial \delta_1} e_{\delta_1}\right)^2 + \left(\frac{\partial v}{\partial \delta_2} e_{\delta_2}\right)^2} \tag{2.16}$$

In the uncertainty calculations for e_u and e_v, twelve partial derivatives are introduced. The equations for these derivatives are included in Appendix C.

Lastly, the error on the absolute wind speed V is established as:

$$e_V = \sqrt{e_u^2 + e_v^2} \tag{2.17}$$

A plot of the error e_V can be observed in Figure 2.6. To calculate it, an accuracy of $\varepsilon_{v_{LOS}} = 1$ m/s is assumed. The other accuracies are neglected. The error is plotted as a function of the azimuth angle difference $\Delta\chi = |\chi_1 - \chi_2|$.

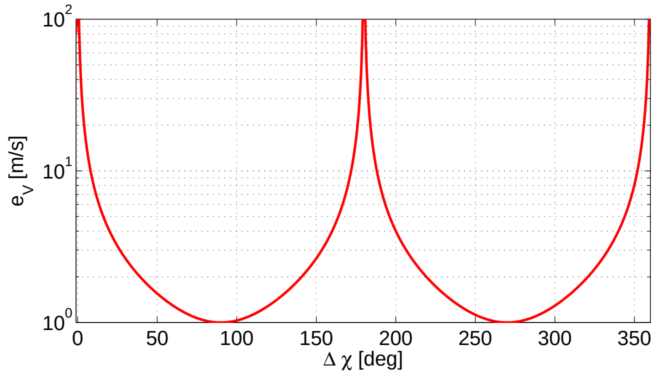

Figure 2.6: *The error e_V as a function of azimuth angle difference $\Delta\chi$.*

This is done to demonstrate one of the most important findings of the error analysis: The error on the absolute wind speed blows up when two LIDARs are measuring along an identical line-of-sight, i.e. when $\Delta\chi = 0°$ or $\Delta\chi = 180°$. When this occurs, both LIDARs are actually producing the same single measurement, making it impossible to evaluate a 2D wind speed vector. The minimum error is reached when LIDARs are pointing under a relative angle of $\Delta\chi = 90°$ or $\Delta\chi = 270°$. Actually, in these cases the error is equal to the only accuracy considered, the $\varepsilon_{v_{LOS}}$ of 1 m/s. Note that the e_V-axis has a logarithmic scale.

2.2.3 Additional Notes

The performed error analysis method is applied on a calculation scheme different from MuLiWEA itself. Although it is able to estimate a comparable structure of the error, the values do not have a particularly high accuracy because of the following shortcomings:

- The error method does not estimate the effect of the specific methods used for interpolating and averaging a set of multiple measurements for one grid point. This could either have positive or negative effects on the error.
- It does not estimate the effect introduced by the continuity equation and thus having an overdetermined linear system. This part of the algorithm is expected to decrease the error.
- It does not include the fact that the 2D LIDAR measurements are not synchronized, neither in time nor space. This is expected to increase the expected error in case the wind field is not steady.

2.3 Validation of the MuLiWEA

The Multiple-LIDAR Wind Field Evaluation Algorithm is validated by comparing the two following wind fields with each other:

- A 10-minute average of a set of simulated 3D wind fields, calculated by the large eddy simulation code PALM [22], describing a single, steady wake, with a resolution of 4 m in all dimensions and a time resolution of 0.4 s.
- The 2D wind field generated by MuLiWEA, applied on 10 minutes of simulated LIDAR measurements within the simulated wind field. A simulation script for virtual LIDAR measurements developed at ForWind is used for this purpose.

The wake of a turbine with diameter D = 62 m and hub height hh = 61 is simulated. The free-stream has a velocity of 9 m/s at hub height and comes from the west. Only the near wake is studied, i.e. the part from the location of the turbine to three turbine diameters downstream.

First the structure of the validation method is presented in Subsection 2.3.1. After that, a comparison between the two mentioned wind fields is made in Subsection 2.3.2. Then, a more quantitative analysis is executed based on the mean absolute error in Subsection 2.3.3. The continuity part of the MuLiWEA is treated separately for the validation afterwards in Subsection 2.3.4. Finally, the validation is concluded in Subsection 2.3.5.

2.3.1 Validation Structure

The simulated wind field is three-dimensional. LIDAR measurement simulations are set up in this volume to make multiple PPI scans. Simulations are done for three LIDARs, placed at different locations, with each of them scanning five PPI planes with different elevations. The LIDAR trajectory parameters of these simulations can be observed in Table 2.2. The letters g, b and r in the first column correspond to the colors green, blue and red, which will later be used in figures to indicate the different LIDARs.

Table 2.2: *LIDAR simulation trajectory parameters.*

LIDAR	Azimuth χ [°]			Elevation δ [°]			Range r [m]		
	Min	Step	Max	Min	Step	Max	Min	Step	Max
1 (g)	50	0.5	80	2.50	1.25	7.50	400	10	850
2 (b)	100	0.5	130	2.50	1.25	7.50	400	10	850
3 (r)	230	0.5	260	2.50	1.25	7.50	400	10	850

To test the algorithm, different horizontal planes can be evaluated by selecting LIDAR measurements in the altitude range $[h-\Delta h\ ,\ h+\Delta h]$ around the height h. Three heights h are regarded in this analysis. Six cases are set up, combining three different altitude selections with two different dual-LIDAR setups. Two additional cases (7,8) are based on case 1 and evaluate the influence of blind spots and course data, respectively. Each of the cases is characterized with the selection of the LIDARs and the measurement plane height in Table 2.3. Here, hub height is indicated by $h = hh$. Furthermore, the parameter $\Delta\chi$ is used to indicate the difference in azimuth between two LIDARs.

Table 2.3: *LIDAR simulation cases description.*

Case	LIDARs	$\Delta\chi$ [°]	h [m]
1	1 (g) and 2 (b)	50	hh
2	1 (g) and 2 (b)	50	$hh + 0.5D/2$
3	1 (g) and 2 (b)	50	$hh + 0.9D/2$
4	1 (g) and 3 (r)	180	hh
5	1 (g) and 3 (r)	180	$hh + 0.5D/2$
6	1 (g) and 3 (r)	180	$hh + 0.9D/2$
7	1 (g) and 2 (b)	50	hh
8	1 (g) and 2 (b)	50	hh

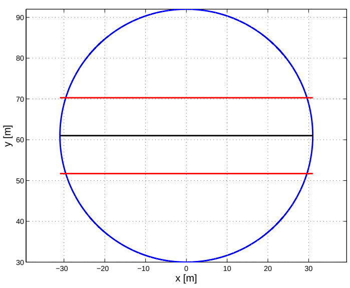

Figure 2.7: *Plane altitude of cases 1,4,7,8.*

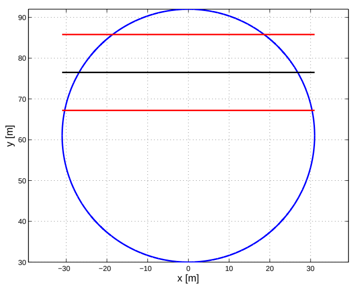

Figure 2.8: *Plane altitude of cases 2,5.*

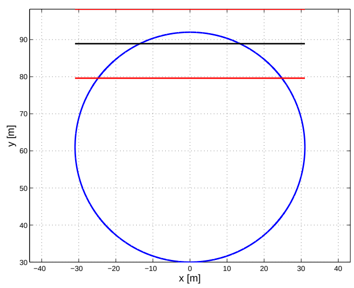

Figure 2.9: *Plane altitude of cases 3,6.*

The different plane altitude selection are illustrated by Figures 2.7-2.9. They show the wind turbine swept area in blue, the height h is indicated with a black line and the red lines indicate $h - \Delta h$ and $h + \Delta h$. In the plots, an arbitrary value for Δh is chosen for illustrative purpose.

Top views of the simulated LIDAR PPI scans can be observed in Figures 2.10-2.13. Large black dots indicate LIDAR positions. The black continuous line encloses the sector in which the PPI is executed. The approximate location of the wake is indicated by a black dashed line. The locations of measurement points are scattered in two distinct colors, corresponding to the color codes in Tables 2.2 and 2.3.

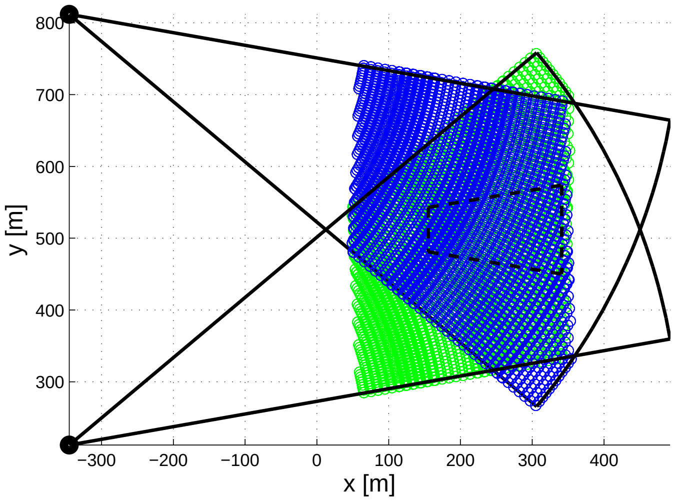

Figure 2.10: *Simulated measurement point scatter of cases 1,2,3 in the validation.*

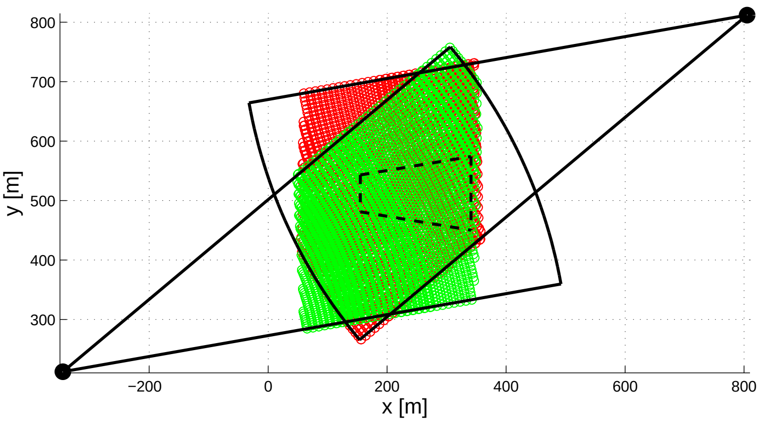

Figure 2.11: *Simulated measurement point scatter of cases 4,5,6 in the validation.*

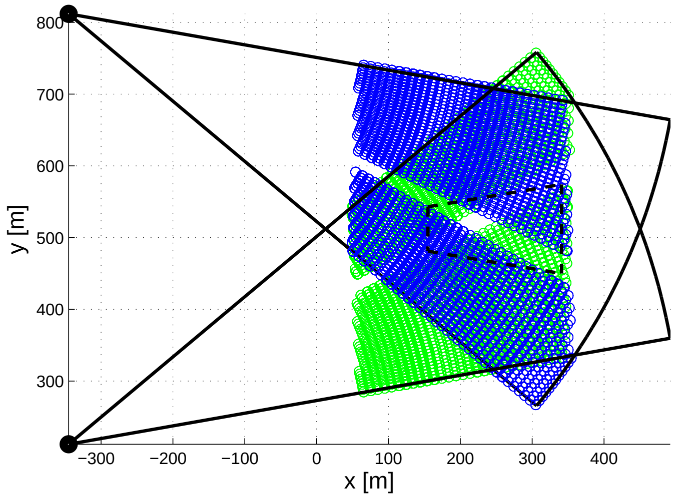

Figure 2.12: *Simulated measurement point scatter of case 7.*

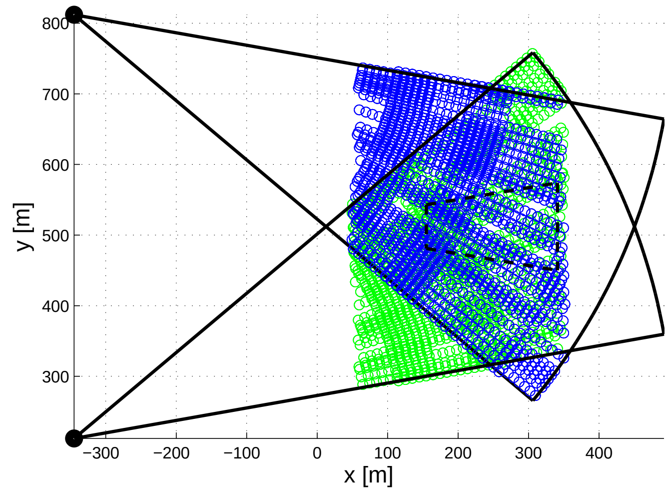

Figure 2.13: *Simulated measurement point scatter of case 8.*

Figures 2.10 and 2.11 illustrate the optimal and non-optimal Dual-LIDAR setup, respectively. The effect of two LIDARs measuring the wind velocity in the same line-of-sight ($\Delta\chi = 180°$) on the numerical error was explained in Section 2.2. Figures 2.12 and 2.13 illustrate the cases 7 and 8 used to investigate the influence of blind spots and course data on the error.

Recall that all LIDAR measurements are done in a volume; the measurements considered for the wind field evaluation at a specific altitude h are spread over multiple LIDAR scanning planes. This is illustrated by the schematic side view in Figure 2.14, which in fact represents a different perspective on case 1 in Figure 2.10.

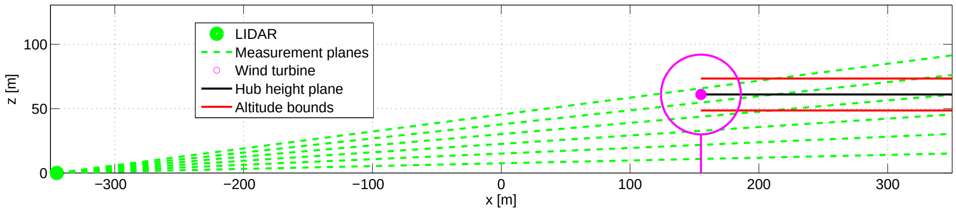

Figure 2.14: *Schematic side view of case 1, displaying the LIDAR 1, the wind turbine, the scanning planes and the selected altitude range.*

In this plot, the selected altitude range is $[hh - 0.3D/2, hh + 0.3D/2]$. This range is indicated with red lines around the black wind turbine hub height line. LIDAR 1 and its scanning planes with different elevations are displayed in green.

Further on in this report, a range of values for the parameter Δh and the radius of influence R are tested in order to optimize these two parameters for a minimum error. To generalize the results, it is convenient to express height offsets in terms of the wind turbine diameter or radius. In this case, a parameter C_h is defined such that $\Delta h = C_h \cdot D/2$.

2.3.2 Comparison of MuLiWEA with Simulated Wind Fields

To validate the algorithm, it is vital that the 2D wind fields evaluated by MuLiWEA are compared with the 3D wind fields simulated by the PALM code. The absolute wind speed and the wind direction, both in the horizontal plane, will be validated separately to cover the two dimensions. After that, the assumption of a negligible vertical wind speed w is assessed by analyzing this third component of the simulated wind field. Finally wake profiles are extracted and plotted separately. All evaluated wind fields in this section are the result of a MuLiWEA execution with a C_h of 0.4 and an R of 8 m. As a result of this parameter selection, between 30 and 70 measurement points K are considered per grid point p for the linear equation in the algorithm. For both the absolute wind speed and the wind direction plots, the first three figures show the simulation results. The figures after that correspond to the evaluated eight different cases. The wake profile plots represent the eight cases, with the evaluated and simulated wake profiles shown in the same graphs.

The simulated absolute velocity wind fields at the three mentioned altitudes can be observed in Figures 2.15-2.17. Below these, the wind fields evaluated by MuLiWEA for all eight cases are visualized by Figures 2.18-2.25.

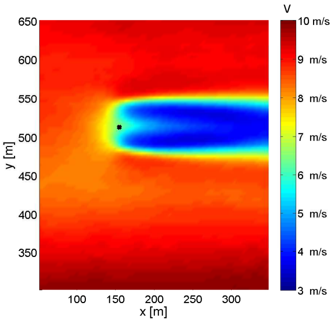

Figure 2.15: *Simulated wind field at hub height.*

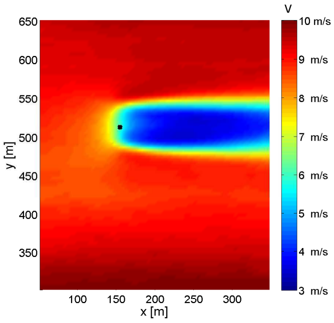

Figure 2.16: *Simulated wind field between hub height and upper blade tip height.*

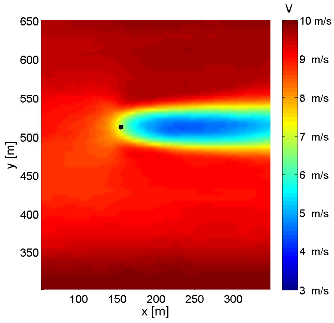

Figure 2.17: *Simulated wind field around upper blade tip height.*

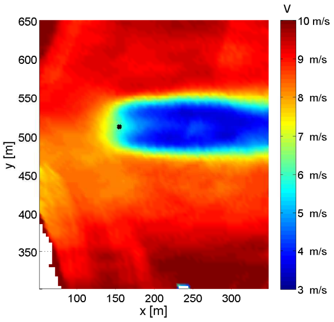

Figure 2.18: *Wind field, case 1.*

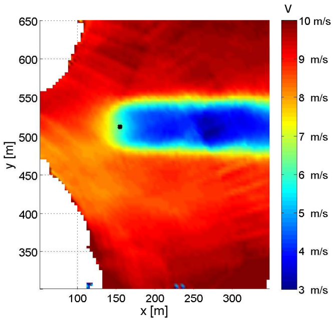

Figure 2.19: *Wind field, case 2.*

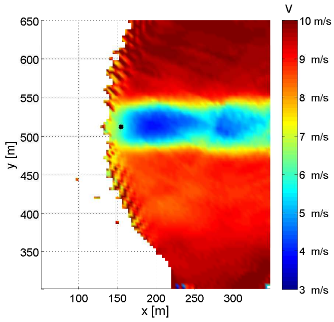

Figure 2.20: *Wind field, case 3.*

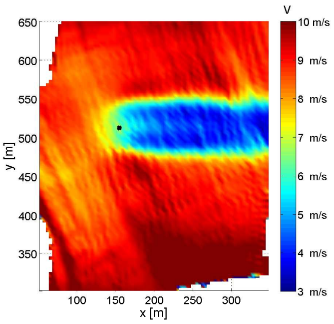

Figure 2.21: *Wind field, case 4.*

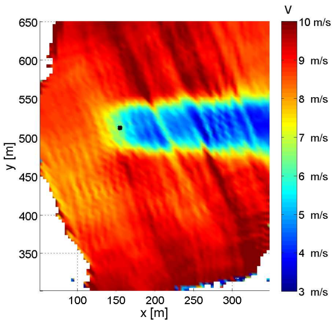

Figure 2.22: *Wind field, case 5.*

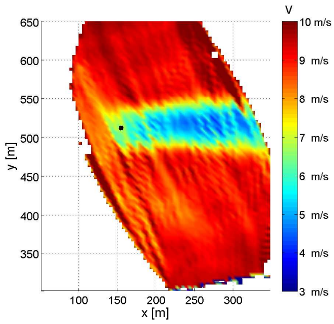

Figure 2.23: *Wind field, case 6.*

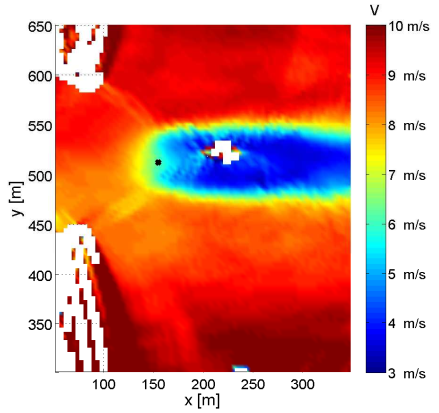

Figure 2.24: *Wind field, case 7.*

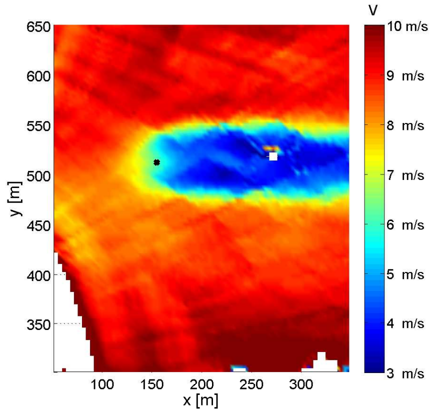

Figure 2.25: *Wind field, case 8.*

First of all, the data gaps at the domain boundaries for some cases are caused by a lack of simulated LIDAR measurements within the selected altitude range. However, in most of the cases the complete near wake is still visible. Both the wake width and center velocity deficit are highest at hub height and decrease at higher altitudes.

The first three cases seem to be able to reproduce the wind field under condition of data availability. However, in case 3 the wake is not able to reproduce the modeled wake width correctly, especially in the near wake. Cases with the non-optimal LIDAR setup (4,5 and 6) are showing strange artifacts. Fluctuations in the wind field are visible as a result of a poorly defined linear system in the main MuLiWEA matrix equation. The case 7 with a blind spot for each LIDAR only shows a gap at the location where the blind spots of the two LIDARs overlap. However, the blind spots clearly leave a footprint in the evaluated wind field (refer to Figure 2.12 for the blind spot locations). Case 8 shows that a wind field can still be evaluated from course data, but the scanning patterns start to appear in the wind field as artifacts. This is a consequence of the measurement interpolation method and the measurement point density.

Figures 2.26-2.28 show the simulated wind fields of the wind direction. After that, Figures 2.29-2.36 visualize the wind fields of the wind direction for all eight evaluated cases.

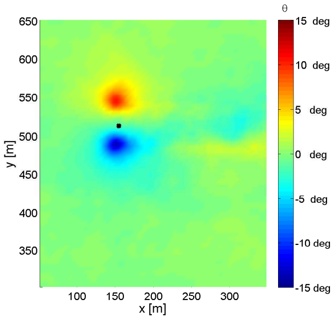

Figure 2.26: *Simulated wind direction at hub height.*

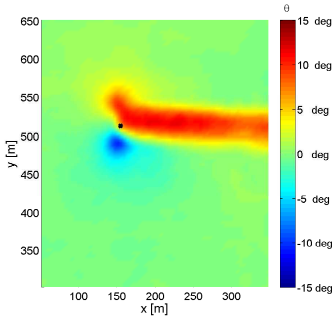

Figure 2.27: *Simulated wind direction between hub height and upper blade tip height.*

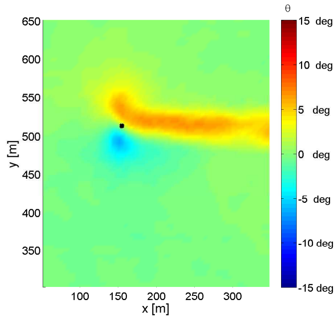

Figure 2.28: *Simulated wind direction around upper blade tip height.*

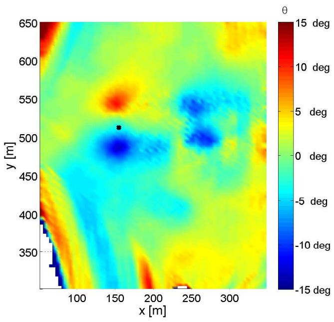

Figure 2.29: *Wind direction, case 1.*

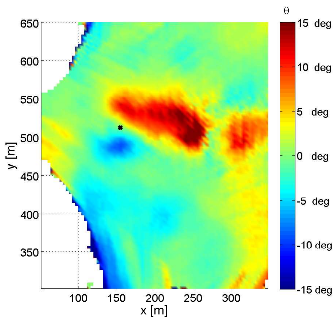

Figure 2.30: *Wind direction, case 2.*

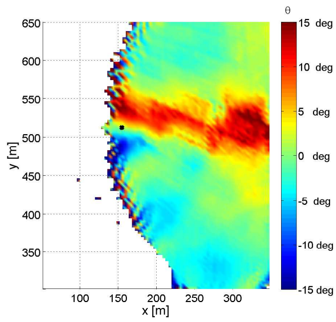

Figure 2.31: *Wind direction, case 3.*

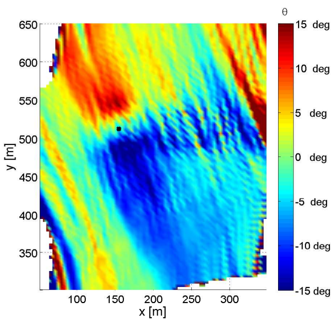

Figure 2.32: *Wind direction, case 4.*

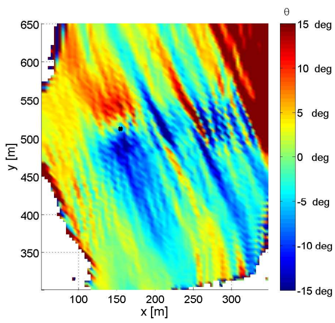

Figure 2.33: *Wind direction, case 5.*

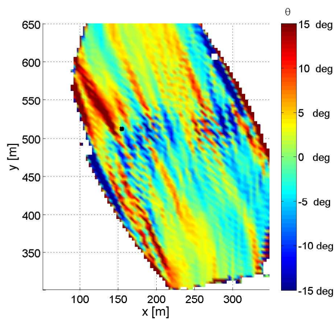

Figure 2.34: *Wind direction, case 6.*

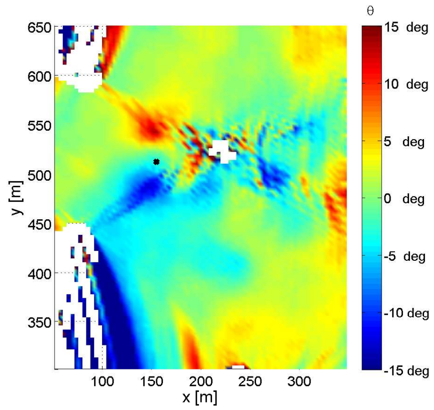

Figure 2.35: *Wind direction, case 7.*

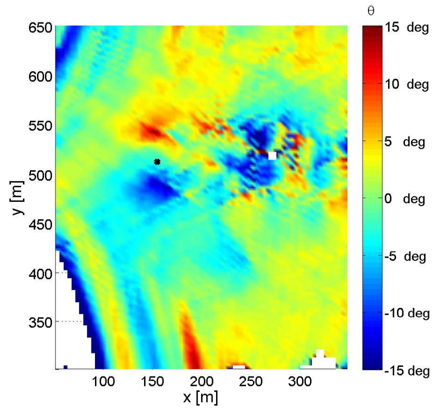

Figure 2.36: *Wind direction, case 8.*

The simulated wind direction plot at hub height (Figure 2.26) shows that the wind is flowing around the wind turbine, which is indicated with a black dot. First, the wind is deflected away from the inflow direction and further downstream it realigns to the main wind direction. For the higher planes (Figures 2.27 and 2.28), a large region of positively deflected wind can be identified. This is a result of the vorticity induced by the rotating blades. The wind field simulates a wind turbine which is rotating clockwise. This means that the vortex behind the rotor will rotate anti-clockwise and indeed cause a vortex which can be observed in the horizontal planes at higher altitudes.

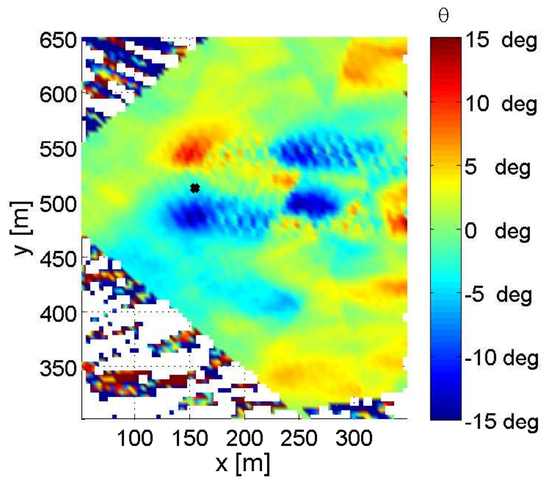

Figure 2.37: *Wind direction, case 1, without continuity adjustment.*

The wind direction field in Figure 2.29 evaluates the initial diversion of the streamlines around the wind turbine correctly, but further downstream it develops some local differences. Namely, a small region with a negative wind direction between -5 and -10° can be observed, where it is supposed to be close to 0. Figure 2.37 shows the same wind direction field as in Figure 2.29, however to generate this plot the algorithm did not apply the continuity adjustment. It is done to illustrate that the local erroneous regions are not a negative side effect of neglecting the vertical transport of momentum as an assumption made for applying the 2D horizontal continuity equation. Namely, both with or without including the continuity adjustment, the same large deviations are produced at the same location.

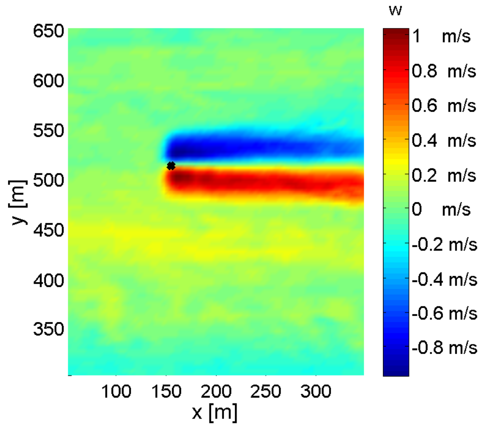

Figure 2.38: *Simulated wind field of the vertical wind speed w.*

A different reason for these errors could be underestimation of the vertical wind speed itself. This can be investigated by means of a simple test. In Figure 2.38 the simulated vertical wind speed field is plotted for case 1. The anti-clockwise vortex mentioned before can be seen clearly. It reaches values between -1 and 1 m/s. When this is neglected, the v_{LOS} estimation is actually off by a value equal to $\sin(\delta)w$. Considering the elevation range of 1.25-7.50° and a vertical velocity of 1 m/s, the error on v_{LOS} will be in the range of 0.02-0.13 m/s. The error of 0.13 m/s is compared with a reasonable absolute wind speed of 5 m/s inside the wake. The order of magnitude of the maximum possible wind direction error can be computed by evaluating $\arctan(0.13/5) = 1.5°$. Clearly, neglecting the vertical wind speed cannot be exclusively responsible for the large deviations in the wind direction of up to 10°.

A likely explanation is finally found by observing the density of the measurements K per grid point p over the grid in Figure 2.39:

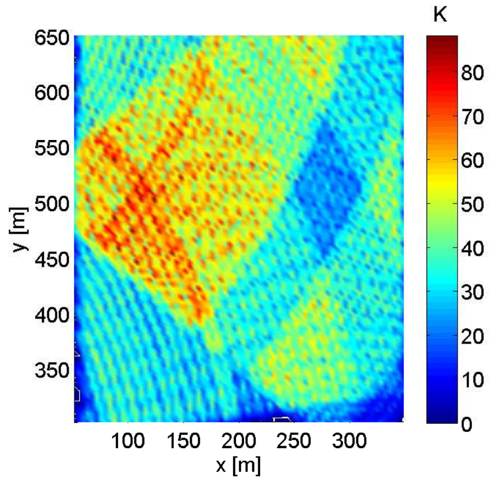

Figure 2.39: *Number of measurements K used per grid point p.*

It can be seen that there is a significantly lower amount of data available exactly at the location of the local errors in Figure 2.29. This is a consequence of combining data from the different PPI planes with different elevations and the intrinsically heterogeneous scanning pattern. When the LIDAR range increases, the distance between the different planes increases and thus the measurement density decreases.

The wind direction plots for cases 2 and 3 (Figures 2.30 and 2.31) shows some local deviations from the simulated profiles in the same vicinity as for case 1. Also the magnitude of the deflection caused by the vortex is overestimated. Cases 4-6 show that the wind field for direction cannot be evaluated properly under the non-optimal LIDAR setup. Where the absolute velocity wind fields are still recognizable as the simulated wind fields, the wind direction fields show significant differences spread throughout the domain. The last two cases 7 and 8 again show some artifacts produced by the data gaps and perform worse than case 1.

The wake profiles extracted from the wind fields for all eight cases can be observed in Figures 2.40-2.47. These profiles are extracted at distances $(0.5D : 0.5D : 3D)$ downstream of the turbine with a total width of $2D$ of each profile. Here D is the turbine diameter. The simulated wake is displayed with red and the evaluated wake is shown in black.

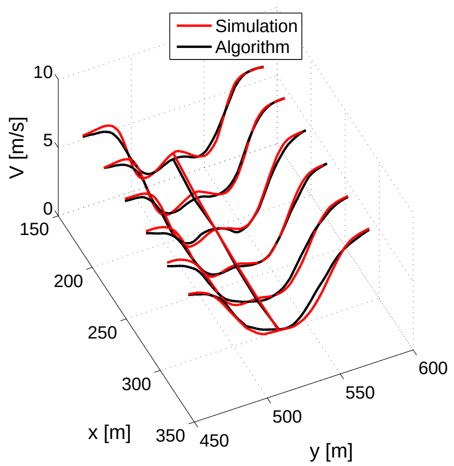

Figure 2.40: *Wake profiles, case 1.*

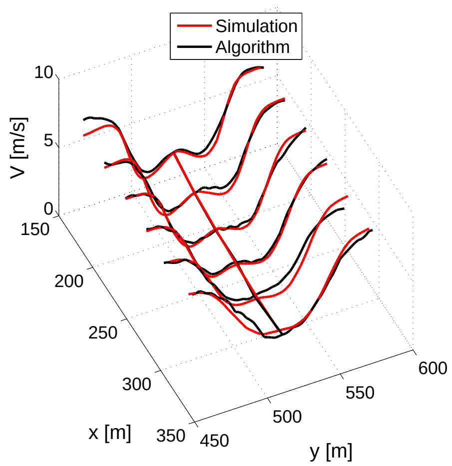

Figure 2.41: *Wake profiles, case 4.*

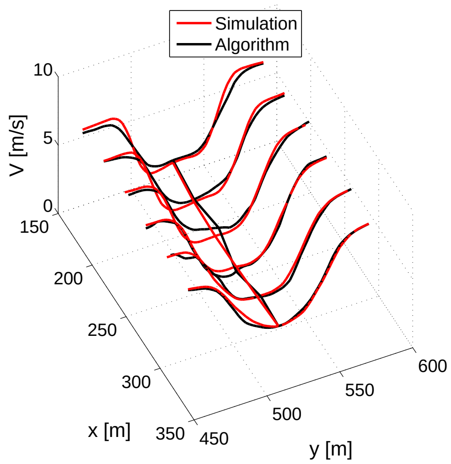

Figure 2.42: *Wake profiles, case 2.*

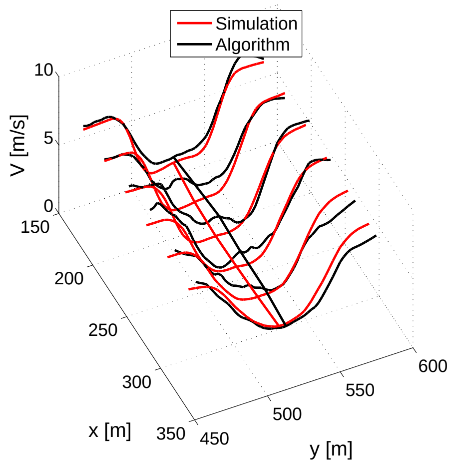

Figure 2.43: *Wake profiles, case 5.*

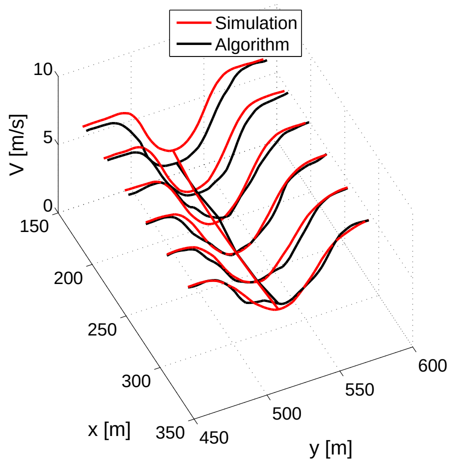

Figure 2.44: *Wake profiles, case 3.*

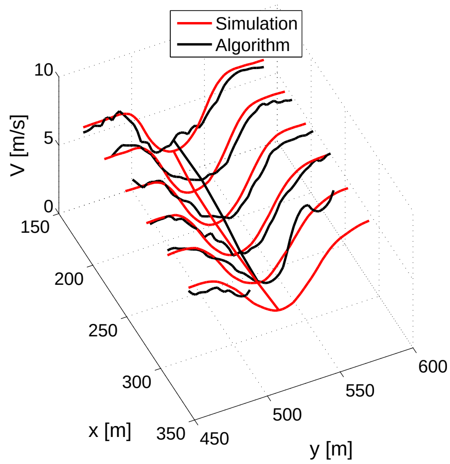

Figure 2.45: *Wake profiles, case 6.*

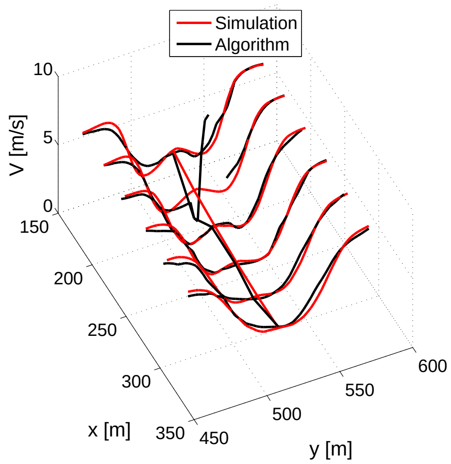

Figure 2.46: *Wake profiles, case 7.*

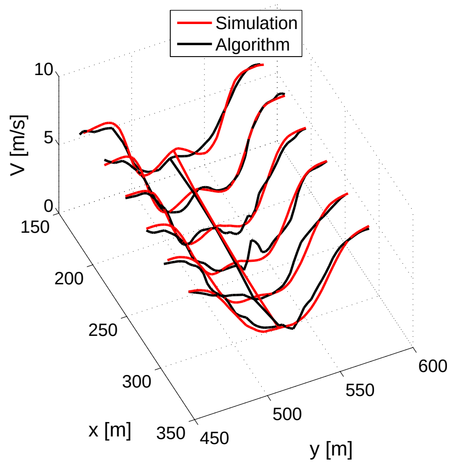

Figure 2.47: *Wake profiles, case 8.*

Observing the plots, it is concluded that cases 1 and 2 show a good match between the simulated wakes and the evaluated wakes. In case 3, especially the width of the first wake profile is not evaluated precisely. MuLiWEA estimates a wider wake than in the actual simulation. This could be a result of mixing measurements from altitudes around the boundary of the wake, i.e. the altitude range covers measurements both inside and outside the wake. It can be noted that the non-optimal LIDAR setup (cases 4-6) provides wake profiles that show large differences to the simulated wind profiles. For the cases with blind spots and course data (7 and 8), some local relatively large errors can be observed in comparison with case 1. In general it is concluded that the wake at hub height can be evaluated more accurately than at higher altitudes and the non-optimal LIDAR setup performs significantly worse than the optimal LIDAR setup.

2.3.3 Analysis on the Mean Absolute Error

The quantitative validation method is based on the mean absolute error (MAE) of the considered three different parameters:

1. The MAE of the absolute wind speed averaged over the total wind field

2. The MAE of the absolute wind speed averaged over the combined set of wake profiles

3. The MAE of the wind direction averaged over the total wind field

Especially the MAE of the wake profiles is an important criterion. Since the maximum measurement error on line-of-sight wind speed by the LIDAR is 0.5 m/s for long ranges (see Table 3.1 in Section 3.1), it is decided that the numerical error should be of the same order. Therefore the following limit is set: For the algorithm and case to be validated, the MAE of both the wind field and the wake profiles should not exceed 0.5 m/s. For the wind direction validation, the value of the MAE should not correspond to a wind speed v-component larger than 0.5 m/s. Keep in mind that for the considered wind field, v = 0 m/s. This criterion corresponds to a maximum MAE on wind direction of $\arcsin(0.5/9) = 3.2°$.

The six cases are evaluated for a radius of influence R in the range 4-12 m and a altitude selection parameter C_h of 0.1-1.0. The MAE is plotted as a function of these two parameters for case 1 in Figure 2.48.

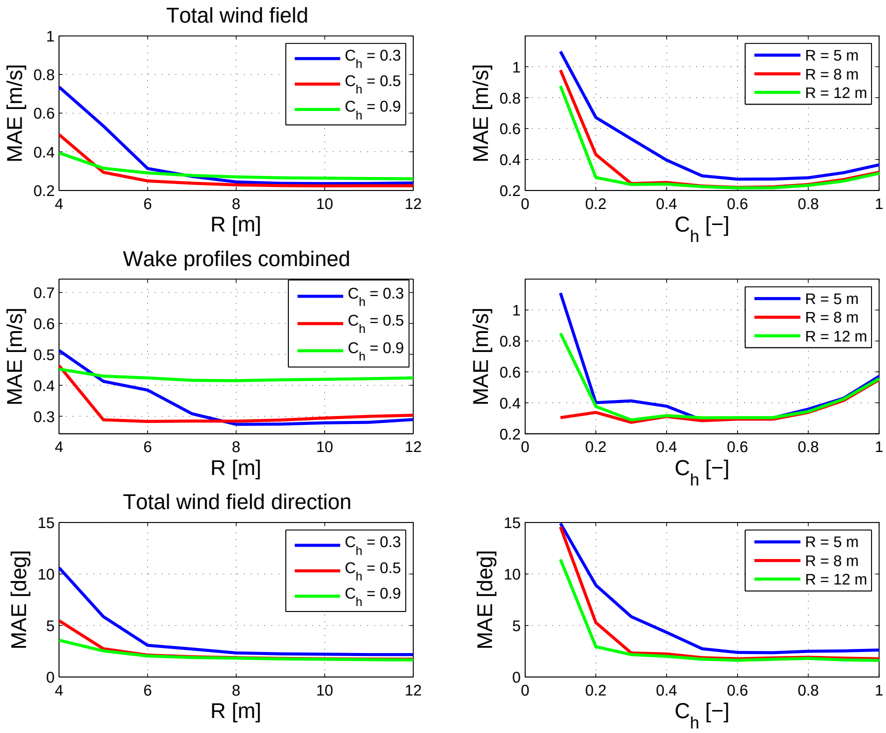

Figure 2.48: *MAE plots as a function of R and C_h for case 1.*

An important conclusion of these plots is that generally, a minimum *MAE* can be found for a specific case, enabling the optimization for the R and C_h parameters. The reasons for the existence of this minimum are:

- There have to be enough measurements available in the altitude range and circle with radius of influence to establish a proper averaged estimate for a grid point

- If the considered measurement selection is too large, gradients in the wake will be smoothed out because of the averaging, so there will be high errors especially at those locations in the wind field where high gradients are found (e.g. wake boundaries). As expected, this phenomenon is mainly affecting the *MAE* of the wake profiles

The latter is illustrated by the absolute error (AE) of the wind field for two different values of C_h, see Figures 2.49 and 2.50. The figure on the right shows relatively high absolute errors on the wake boundaries, due to the large C_h of 0.9.

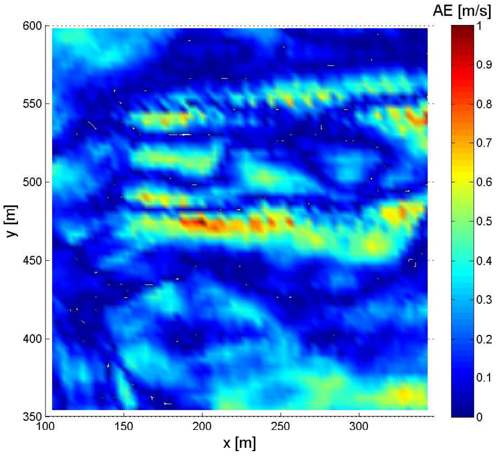

Figure 2.49: *AE of the wind field of case 1, with R = 8 [m] and C_h = 0.3.*

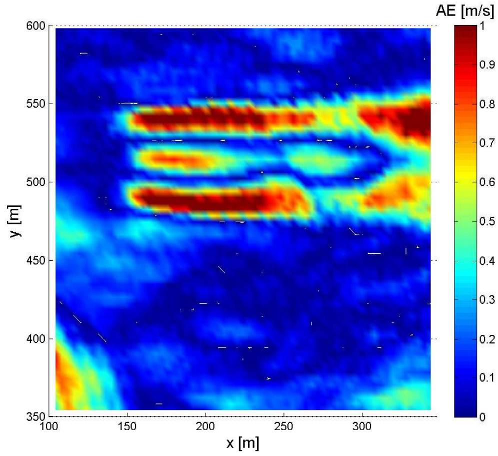

Figure 2.50: *AE of the wind field of case 1, with R = 8 [m] and C_h = 0.9.*

Theoretically, the equilibrium between these two considerations yields a minimum MAE for the corresponding combination of R and C_h. These optimized parameters can be observed in Table 2.4. Note that different minima are found for the MAE of the total wind field velocity and direction and of the wake profiles in particular. As said, the latter are considered most important for the validation of the algorithm.

Table 2.4: *Optimized parameters and minimum MAE for the different cases.*

Case	Wind field			Wake profiles			Direction		
	R_{opt} [m]	$C_{h_{opt}}$ [-]	MAE_{min} [m/s]	R_{opt} [m]	$C_{h_{opt}}$ [-]	MAE_{min} [m/s]	R_{opt} [m]	$C_{h_{opt}}$ [-]	MAE_{min} [°]
1	8	0.6	0.18	5	0.1	0.22	12	0.6	1.29
2	12	0.3	0.21	9	0.3	0.21	12	0.6	1.50
3	11	0.4	0.36	8	0.2	0.39	12	1.0	2.14
4	10	0.7	0.31	10	0.3	0.23	12	1.0	3.48
5	10	1.0	0.37	11	0.3	0.46	12	0.6	5.02
6	12	0.8	0.39	12	0.5	0.38	12	0.4	3.24
7	12	0.5	0.22	6	0.1	0.24	12	1.0	1.82
8	10	0.6	0.22	8	0.3	0.27	12	1.0	1.61

The first observation from Table 2.4 is that no minima can be found for the wind direction MAE, yet it converges for larger parameters. Namely, the lowest MAE is always found for the highest evaluated R of 12 m. The reason is that the errors in direction are mostly a *local* effect and the MAE is smoothed out by taking into account a larger volume of the wind field for measurement interpolation.

Regarding the wake profiles MAE, the optima are located at higher values of R and C_h for the non-optimal LIDAR setup cases with $\Delta\chi$ = 180°. Because the linear system in the Multiple-Doppler algorithm is not well defined for these cases, more measurements taken into account means that the matrix equation yields a more stable solution.

Apart from these observations, no solid conclusion can be drawn from the optimization of parameters R and C_h. The results do not seem to follow a clear pattern and therefore an other approach is used. In order to have a better direct comparison, all cases are evaluated for the MAE for the specific set of parameters R = 8 and C_h = 0.4. These values have been chosen, because the MAE values do not improve significantly anymore when increasing them (See 2.48). This allows for an objective comparison of the different cases. The results can be observed in Table 2.5.

Table 2.5: *MAE values of all cases, for R = 8 and C_h = 0.4.*

Case	MAE (field) [m/s]	MAE (profiles) [m/s]	MAE (direction) [°]
1	0.19	0.23	1.76
2	0.22	0.25	1.89
3	0.36	0.42	2.65
4	0.40	0.26	5.58
5	0.47	0.54	6.53
6	0.51	0.43	3.87
7	0.26	0.31	2.57
8	0.25	0.31	2.24

The following conclusions can be drawn from this table:

- The cases with an non-optimal LIDAR setup (4, 5 and 6) have a relatively high error. In fact, these three cases are the only ones that do not fulfill the three imposed validation criteria. For all three cases, the wind direction MAE is larger than 3.2°. Case 5 has a wake profile MAE that exceeds 0.5 m/s and case 6 has a wind field MAE larger than 0.5 m/s in addition to that

- Cases that consider planes at upper wind tip height (3 and 6) have a relatively high error compared to other evaluation planes. A possible explanation is that the altitude range will contain LIDAR measurements from both inside and outside the wake, which will be averaged to evaluate the wind field inside the wake

2.3.4 Influence of the Continuity Adjustment

Since the implementation of a continuity adjustment is an important part of the MuLiWEA, it is necessary to assess its influence. Therefore the evaluated wind fields for cases 1 and 4 are analyzed with and without the continuity implementation. Again, the parameters R = 8 m and C_h = 0.4 are used. In Figures 2.51-2.54, the evaluated wind fields can be observed.

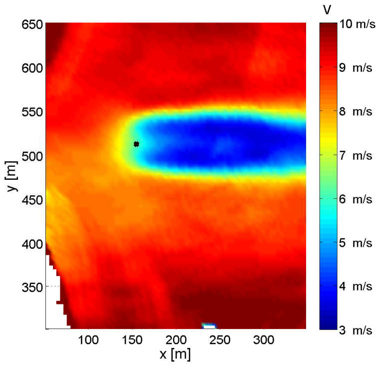

Figure 2.51: Evaluated wind field for case 1, with continuity.

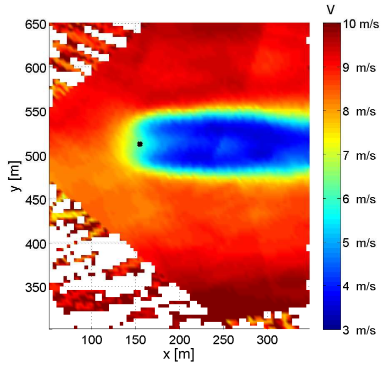

Figure 2.52: Evaluated wind field for case 1, without continuity.

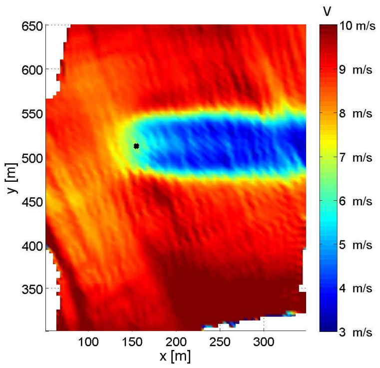

Figure 2.53: Evaluated wind field for case 4, with continuity.

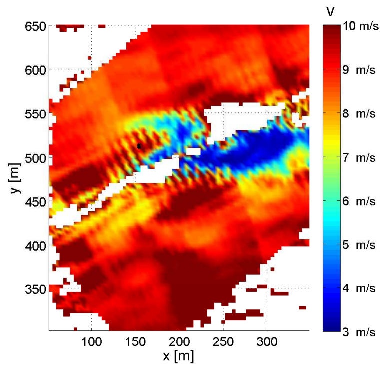

Figure 2.54: Evaluated wind field for case 4, without continuity.

Significant differences can be observed between the plots with and without continuity adjustment. In Figure 2.52, the boundary between the fully recovered wind field and the part of the field that is missing data corresponds to the boundary of the plane in which the PPI scans of the two LIDARs overlap (see Figure 2.10 for the PPI scan structure). In Figure 2.54, it can be seen that no wind field is evaluated in the vicinity of the line that is described by $\Delta\chi = 180°$, as pointed out in the error analysis (Section 2.2). See also the PPI scan structure in Figure 2.11. In general, it can be said that including the continuity equation enables a solution at locations where the main matrix equation of the MuLiWEA is ill-defined. This happens when the LIDARs are measuring in the same line-of-sight ($\Delta\chi = 180°$) or when data from only one LIDAR is available.

Table 2.6: *MAE values of cases 1 and 4, for R = 8 and C_h = 0.4, with and without continuity adjustment.*

Case	*MAE* (field) [m/s]	*MAE* (profiles) [m/s]	*MAE* (direction) [°]
With continuity adjustment:			
1	0.19	0.23	1.76
4	0.40	0.26	5.58
Without continuity adjustment:			
1	0.26	0.23	2.59
4	0.94	1.14	12.91

In Table 2.6, the *MAE* values for the two cases executed with and without continuity adjustment can be found. It can be seen that including the continuity equation significantly improves the solution, especially for case 4. However, for this case the improvement is not enough to pass the validation requirement stated before.

2.3.5 Conclusion

The final conclusion of this validation is that the MuLiWEA is functioning appropriately thus valid under the conditions of an optimal Dual-LIDAR system setup, evaluating the wind field at hub height. Also data that includes blind spots or course data can be considered, though with care. Data sets in which two LIDARs have the same line-of-sight ($\Delta\chi$ = 180°) should be avoided. This was already expected from the error analysis in Section 2.2. The continuity equation implementation in MuLiWEA provides an improved solution of the wind field even with this non-optimal LIDAR setup, but in this case the solution is still not accurate enough.

The knowledge acquired in this chapter on the general influence of the algorithm parameters C_h and R can be applied to real measurement cases, but care has to be taken. The parameter C_h is normalized, such that it proves to be a good estimate. The parameter R is not normalized, so this will be dependent on the density of measured points. It has to be noted as well that no measurement error was simulated for the validation wind field. In reality there are measurement errors that could be smoothed out partly by the numerical process. The quantitative impact of this effect on the optimal R parameter is not known. It is expected that for real cases, more measurements are needed per grid point to reach the same accuracy as the validation wind fields.

Although the evaluated absolute velocity wind field generally has a good accuracy compared to the simulated wind field, the wind direction field is more likely to have local errors. First of all, in the considered case u is the main wind component and the wind component v is close to zero. Errors on v have a significantly higher relative impact than errors on u. Secondly, the specific multiple-PPI scanning pattern causes a heterogeneous measurement point density over the grid and significant errors are introduced when the number of points used per grid point is not sufficient.

A small check was done on the assumption of the negligible vertical wind speed component w. It was found that this is not likely to cause high errors in the wind field and thus it is a valid assumption to make. However, the simulation was done regarding neutral atmospheric conditions. Care has to be taken when the prevailing atmospheric condition differs from this and vertical temperature gradients are more likely to occur, which affect the vertical wind speed.

3 Application of the MuLiWEA

In this Chapter, the developed MuLiWEA will be applied to measurement data. First, the measurement campaign will be introduced in Section 3.1. Information will be given about the wind farm and the installed LIDARs. The sources of the measurement data and validation data are listed and the used software is mentioned. Lastly, wind fields evaluated by MuLiWEA will be compared to wind fields calculated by wake simulations in Section 3.2.

3.1 Experimental Campaign

The experimental campaign can be divided into two main elements:

- The hardware setup, i.e. the LIDAR scanners and the wind farm
- The software element, i.e. the data chain

First, the used type of LIDAR will be characterized. Then the wind farm layout including the locations of the LIDARs will be visualized. Limitations of the system configuration will be discussed. Finally, it will be made clear how the data is collected and processed.

3.1.1 LIDAR System

ForWind installed three LIDARs of the type Windcube WLS200S in the »alpha ventus« wind farm. These are long-range, pulsed LIDARs. An overview of the LIDAR specifications can be observed in Table 3.1.

As mentioned before, 10-minute average wind fields are ultimately evaluated from overlapping PPI scans. The 10 minutes are needed to collect sufficient data to apply the MuLiWEA. Generally it takes between 2 to 5 minutes to perform a PPI scan with the LIDARs. However, this highly depends on the size and the density of the area covered by the scan, i.e. the width of the azimuth range and the step size. Detailed information will be given when evaluating a case in the next section.

Table 3.1: Technical sheet of the Windcube WLS200S.

Properties		
Wave length	1.54	μm
Pulse length (FWHM)	0.1 - 0.4	μs
Max laser power	5	mW
Pulse repetition rate	10-20	kHz
Max range	6500	m
Acquisition		
Photodiode sampling rate	250	MHz
FFT length	64 - 128 - 256	points
Accuracy v_{LOS}	0.2 (r< 2 km) - 0.5 (r> 2 km)	m/s
Max # range gates	240	-
Scanner		
Type	2	DOF
Angular resolution	0.01	deg
Pointing resolution	0.1	deg
Max angular speed	30	deg/s

3.1.2 Layout of the Wind Farm

The »alpha ventus« wind farm is located approximately 44 km north-west of the German island Borkum, in the North Sea. It is characterized by a regular 4-by-3 array of wind turbines, with a total rated power of 60 MW. Two different manufacturers supplied the wind turbines, i.e. the six northern turbines are REpower 5M and the six southern turbines are AREVA M5000-116. The specifications of these two wind turbine types are included in Table 3.2 [4]. As can be seen from this data, the two wind turbine types are highly similar to each other in terms of dimension. The most significant difference is the substructure they are using.

Table 3.2: Specifications of the wind turbines [4].

Turbines Type	AV1 - AV6 REpower 5M	AV7 - AV12 AREVA M5000-116
Substructure	Jacket	Tripod
Hub height hh [m]	92	90
Rotor diameter D [m]	126	116
Rated power P [MW]	5.0	5.0
Cut-in wind speed [m/s]	3.5	3.5
Rated wind speed [m/s]	13	12.5
Cut-out wind speed [m/s]	30	25

A layout of the wind farm and the LIDAR system setup is plotted in Figure 3.1. The coordinate system is centered around the geometrical wind farm midpoint. The twelve turbine positions are indicated with black dots and their names AV1 - AV12.

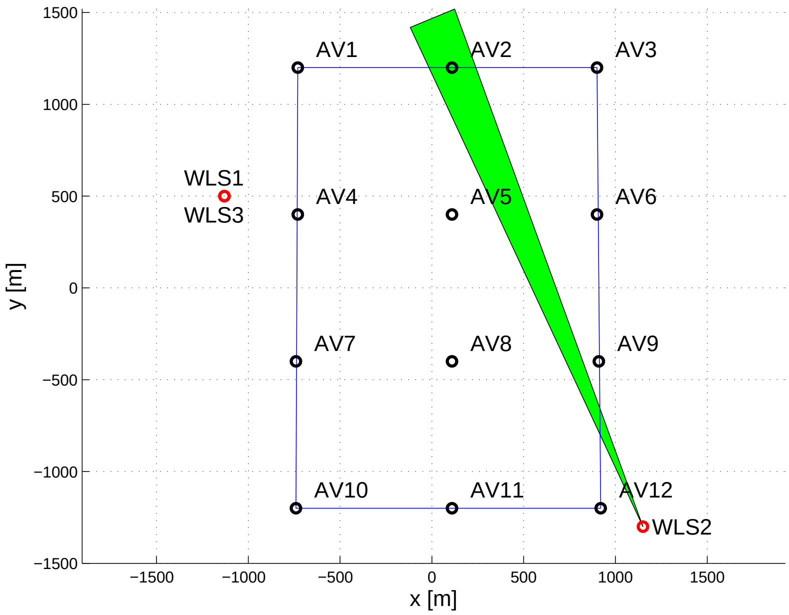

Figure 3.1: *Setup of the »alpha ventus« wind farm and the Multi-LIDAR system, including its largest occurring blind spot.*

The Multi-LIDAR system used by ForWind in the wind farm »alpha ventus« consists of three LIDARs, which will be referred to as WLS1, WLS2 and WLS3. The LIDAR positions are indicated with red dots. WLS2 is placed on the transformer platform in the south-east corner of the wind farm. WLS1 and WLS3 are both placed on the FINO1 support platform near the north-west corner of the wind farm. Note that these two LIDARs appear as one red dot, because of the close placement and the scale of the picture.

This specific setup of the LIDAR system has several limitations and consequences as a function of the offshore environment. The most important ones are listed here:

- There are hard targets in the wind farm, e.g. masts and the wind turbines themselves. When in the line-of-sight of the LIDARs, these will obstruct their view in so-called blind spots. The largest and therefore most limiting blind spot of WLS2 is indicated with a green patch in Figure 3.1. It is caused by a pole on the transformer platform, close to the LIDAR lens.

- Two out of three LIDARs (WLS1 and WLS3) are placed on the same location. This limits the possibilities of executing multiple overlapping PPI scans. Additionally, it is not possible to execute synchronized single 3D vector measurements, but this is not a limiting factor for the scope of this thesis.

- Since the LIDARs are placed close to the sea surface, there are limitations to retrieving measurement at hub height with PPI scans. Combining a low elevation angle with a long range, PPI scans can be done such that a part of the measurements are located within a sufficiently small altitude range centered around hub height. A different approach is to scan and then combine multiple PPI scans with different elevations. This has been investigated during the validation of MuLiWEA in Section 2.3.

- Under specific weather conditions such as mist or heavy rain, the LIDARs are not able to measure with sufficient accuracy, due to laser beam scattering by the water drops in the air. A significantly low *CNR* will be recorded for the measurements in this case.

- Since a large error increase occurs for the azimuth difference $\Delta\chi = 180°$ (see Section 2.2), the wake of e.g. AV8 cannot be characterized with sufficient accuracy (see Figure 3.2). The optimal accuracy is reached when scanning under a relative angle of $\Delta\chi = 90°$, e.g. scanning the wake of AV3 or AV10.

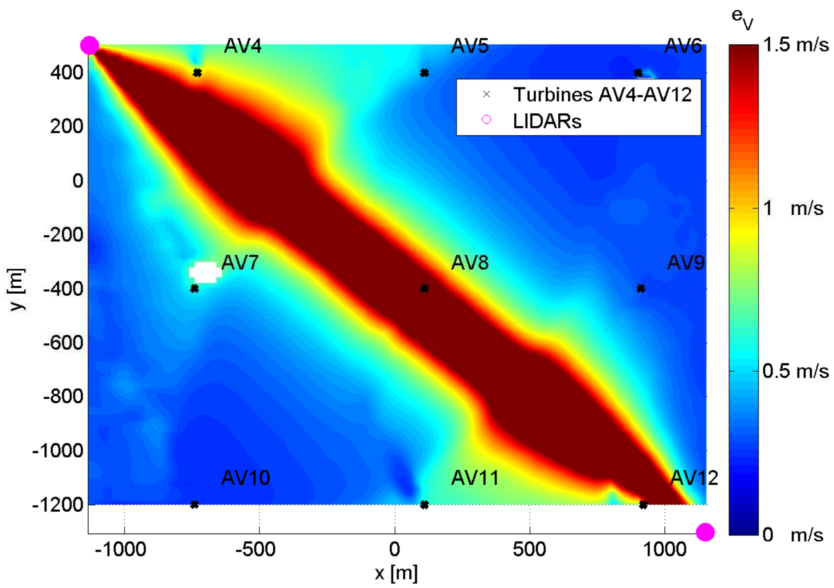

Figure 3.2: *Estimated maximum error e_V on the calculated absolute wind speed.*

In Figure 3.2, the maximum expected error e_V is plotted for the major part of the wind farm (see also Figure 3.1 for the wind farm layout). The LIDAR locations are in the north-west and the south-east corners of the plot. It can be seen that the error blows up on the line that connects the two LIDAR locations. This effect was evaluated in Section 2.2. LIDARs measuring with a relative $\Delta\chi$ of $180°$ actually just provide a single measurement. Note that the color scale is topped at 1.5 m/s, because the error calculation reaches a singularity on the line with $\Delta\chi = 180°$ and the scale would not be able to show variations in the low error regions.

3.1.3 Data Chain

For the scope of this master thesis, four sources of data are used for analysis:

1. Measurement data from the LIDAR scanners, supplied by ForWind. This forms the main data, needed for evaluating wind fields and characterizing wakes with the MuLiWEA algorithm.

2. Meteorological data from the FINO1 mast [20], to serve as input for the wake model that is used for validation. Namely, the cup anemometers and the wind vanes at 33 m and 90 m (hub height) providing the wind speed and the wind direction, respectively. The 10-min statistics of these data sets, along with the ones of the air temperature at 30 m and the water surface temperature measured by a buoy, were considered to calculate the Monin-Obukhov length.

3. SCADA data from AREVA Wind GmbH for the AV10 turbine, in particular the wind direction provided by the wind vane installed on top of the nacelle.

4. AREVA M5000-116 wind turbine thrust coefficient curve, needed as input for the wake model.

An overview showing the contents of the different data used for analysis is presented in Table 3.3. The sources refer to the ones listed before.

Table 3.3: *Data variables used for analysis.*

Source	Variable	Meaning
1	t	Time stamp
	χ	Azimuth angle
	δ	Elevation angle
	r	Range
	x, y, z	Cartesian coordinates
	v_{LOS}	The line-of-sight wind speed
	CNR	Carrier-to-Noise Ratio
2	V	Absolute wind speed at 33 and 90 m
	σ_V	Standard deviation of V at 33 and 90 m
	θ	Wind direction at 33 and 90 m
	T_a	Air temperature at 30 m
	T_w	Water surface temperature
3	γ	Relative wind direction on the nacelle
4	C_T	Thrust coefficient

An overview of the software used to process this data is listed below:

- MathWorks MATLAB R2013a is used as the main tool to read and write data, effectively perform large calculations and execute some simulations. The MuLiWEA algorithm is implemented in MATLAB.

- FLaP, a wake modeling software developed at the University of Oldenburg [19].

- AMOK 1.0.3, developed at DTU Risø by S. Ott. It is used to characterize atmospheric stability by means of calculating the Monin-Obukhov length. The theory behind this software is explained under the name Monin-Obukhov method in [13].

The LIDAR campaign at »alpha ventus« was executed during the time period from August 2013 until March 2014. The LIDAR measurements v_{LOS} are accompanied by the time of measurement and the location of the measurement in 3D coordinates. Both the Cartesian coordinates x, y, z and the geographical coordinates χ, δ, r are relevant for the research. The CNR value has been introduced in Section 1.3 and can be used to select data based on accuracy. The CNR is calculated internally by the LIDARs. In this research, measurements are filtered at both sides of the CNR range: A low CNR indicates that the signal is scattered, e.g. due to fog, and the evaluated v_{LOS} will have a large error. On the other hand, a significantly high CNR can indicate a hard target, which acts as a reflector. Static hard targets such as poles and wind turbine towers will result in a v_{LOS} of 0 m/s, but moving hard targets such as wind turbine blades could produce a v_{LOS} much higher than the wind speed itself. These local outliers are undesired.

At the FINO1 mast [20], the wind speed and its standard deviation are measured at various heights. This enables for the calculation of the turbulence intensity TI, which is an input for the wake model. Also air and water surface temperatures are needed for processing with the software tool AMOK in order to characterize the atmospheric stability with the Monin-Obukhov length L.

The thrust coefficient C_T applied in the Ainslie wake model [2] was evaluated by means of aeroelastic simulation of a wind turbine model provided by AREVA Wind GmbH.

A catalog of measurement data is built. It can be observed in Appendix D. Different LIDAR measurement scenarios are executed and these are split up in sets containing a few hours of data. The data sets contain the name of the scanning scenario, corresponding to the name used in the LIDAR measurement database on the ForWind server. Furthermore the time domain, the prevailing wind direction, the visible turbine wakes, the measurement altitude, the considered LIDARs, the quality of the data and some notes are provided. Some of the cases have been removed, leaving blank spaces in the table. An important note is that, ideally, the wakes are specified at hub height of the wind turbine. Data sets with the term 'HH' for the altitude specification contain enough measurements within a reasonable altitude range centered around hub height to be useful. Scattered altitude means that the differences in altitude are too high to be processed in a reliable manner. Low altitude indicates that there are measurements in a reasonably narrow altitude range in the low altitude ranges, i.e. around lower blade tip height or lower. These measurements might be taken in the lower region of the wake or even below the wake. Particularly useful data sets are marked in green.

Based on the catalog, data sets can be selected for analysis and comparison with a wake model. There are limitations on the usefulness of data sets:

- Only data sets with sufficient measurements taken within a reasonably small altitude range centered around hub height are useful.
- Some data sets are characterized by low CNR values due to bad weather conditions and do not contain enough data to characterize a wake with sufficient accuracy.

- In some scenarios, the wake is located outside of the overlapping LIDAR scan area. This happens when relatively small azimuth sectors are scanned because of time considerations and if - at the same time - the wind direction varies from the weather forecast that is used to plan the scanning scenario.

- Only data of the AREVA Wind GmbH turbines are available for this research. Therefore only turbines AV7 - AV12 can be considered.

Because of these reasons, only one scanning scenario is left to be used for analysis, spread over cases 21-24 in the catalog.

3.2 Comparison of MuLiWEA Results with FLaP Wake Model

To have a better understanding of the FLaP wake model principles and the comparison of evaluated wakes with this model, first a concise description of this wake model is provided. It focuses on the input parameters and their qualitative effect on a wake. After that, the scenario selected for analysis will be described and characterized thoroughly, in terms of parameters used for the analysis by MuLiWEA and the atmospheric conditions during the time intervals. Lastly, the comparison between the wake profiles evaluated by MuLiWEA and those modeled by FLaP is presented for the selected cases.

3.2.1 Notes on the FLaP Wake Model

The program FLaP [19] is based on the Ainslie wake model [2]. This model was already mentioned in Section 1.3. In this model, an initial Gaussian shaped velocity deficit at a downstream distance of $2D$ is calculated as a function of the wind turbine thrust coefficient C_T. Both the initial velocity deficit and the wake width increase with the C_T.

An example thrust coefficient curve (Figure 3.3) was calculated by running a simple Blade Element Momentum optimization code on the NREL 5MW reference turbine rotor [17]. It is used to give a qualitative understanding of the C_T parameter and its effect on wake characteristics. In the wind speed region below the rated speed of approximately 11 m/s, the C_T has a high value as a consequence of optimizing the power output of the wind turbine. For higher wind speeds, the C_T is lowered by pitching the blades of the turbine to keep the power output at rated level. Based on this knowledge, it can be concluded that atmospheric wind speeds higher than the rated speed will result in a relatively low initial velocity deficit and a smaller wake expansion.

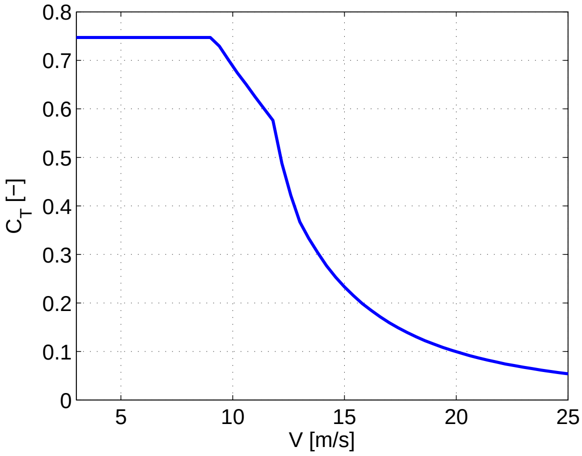

Figure 3.3: *General shape of a C_T curve.*

Important atmospheric condition inputs are the turbulence intensity TI and the Monin-Obukhov length L, which is a quantitative measure of atmospheric stability. Table 3.4 presents the stability classes based on the L parameter as presented by Hansen [13]:

Table 3.4: *Overview of the atmospheric stability classes [13].*

Class	Obukhov length [m]	Atmospheric stability class
cL=-3	-100 ≤ L ≤ -50	Very unstable (vu)
cL=-2	-200 ≤ L ≤ -100	Unstable (u)
cL=-1	-500 ≤ L ≤ -200	Near unstable (nu)
cL=0	|L|>500	Neutral (n)
cL=1	200 ≤ L ≤ 500	Near stable (ns)
cL=2	50 ≤ L ≤ 200	Stable (s)
cL=3	10 ≤ L ≤ 50	Very stable (vs)

The turbulence intensity influences the width of the wake and how quickly the wake recovers. A high TI causes more mixing of the air between the wake and the ambient air and therefore a quicker wake deficit recovery. Also the initial velocity deficit at a $2D$ distance is smaller for a higher TI. A similar effect can be caused by unstable stratification. This condition is characterized by vertical temperature gradients, causing thermal mixing of air in that direction. Therefore unstable cases have a quicker wake recovery, while for neutral and stable cases the wake will be relatively long.

3.2.2 Characterization of the Selected Scenario

As stated before, cases 21-24 from the catalog will be evaluated. The internal name of this scenario is 'WAKEAV01andWAKEAV0301'. It describes an overlapping PPI of the LIDARs WLS2 and WLS3, scanning the single wake of AV10. Refer to Figure 3.1 for the LIDAR and turbine positions. The scanning scenario is executed during the whole day 2014-02-20. Different requirements for the available data act as a filter for useful time intervals within this data set:

- The 10-minute average offset between the wind direction of the wind turbine inflow and yaw of wind turbine AV10 cannot exceed 3 degrees. Otherwise the wake might have a deflection and this cannot be modeled by FLaP. It is assumed that the measured relative wind direction on top of the nacelle γ represents this offset.
- There has to be a sufficient amount of data from both two LIDARs with a reasonable CNR for an accurate measurement. The selected CNR range is between -22 and -4 dB.
- The relevant FINO1 data set (listed in Table 3.3) has to be complete. When there are gaps in the meteorological data, the corresponding time interval cannot be modeled and thus will not be used.

In total, fifteen different 10-minute intervals of data fulfill all these requirements and are considered useful for the analysis. The relevant conditions of these data sets can be observed in Table 3.5. It contains the starting time of the 10-minute interval, the wind speed V at hub height, wind direction θ at hub height, turbulence intensity TI, AV10 relative wind direction on the nacelle γ and the Monin-Obukhov length L. The selected altitude range is $[hh - C_h D/2, hh + C_h D/2]$ with a C_h of 0.3, which corresponds to an altitude range of [72.6, 107.4] m.

Table 3.5: *Specification of the relevant data sets for wake model comparison.*

Interval	Start time	V [m/s]	θ [deg]	TI [%]	γ [deg]	L [m]
1	01:00:00	10.1	217	6.3	1.0	1590
2	01:10:00	9.3	217	6.5	0.6	5236
3	01:30:00	10.5	214	5.6	2.1	-2083
4	05:40:00	11.1	186	5.6	-2.2	-496
5	06:10:00	10.5	179	5.6	-0.2	-297
6	06:20:00	10.9	181	5.4	-0.1	-305
7	06:30:00	11.1	181	6.1	1.2	-320
8	06:40:00	11.2	182	5.9	2.9	-312
9	06:50:00	11.7	183	5.3	0.8	-301
10	07:00:00	11.8	182	5.3	-1.1	-301
11	07:10:00	11.7	180	5.8	-3.0	-282
12	07:20:00	11.8	179	5.4	-2.3	-315
13	21:40:00	15.8	184	4.2	-2.6	293
14	21:50:00	15.9	187	5.0	-0.6	260
15	22:00:00	16.0	188	5.0	-0.8	301

The prevailing wind during the scanning time frame is coming from the south or the south-west. The values of the Monin-Obukhov length L cover mostly near stable and near unstable atmospheric stratification (refer to Table 3.4). Turbulence intensities between 4.2 and 6.5 % are found.

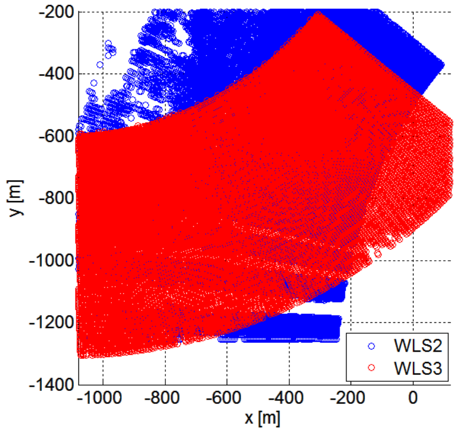

Figure 3.4: *Top view of the measurement points of both LIDARs.*

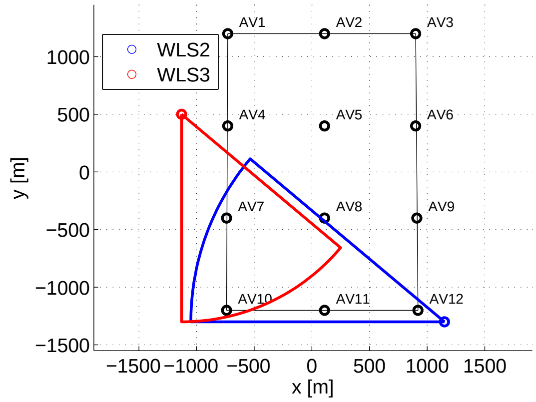

Figure 3.5: *Top view of the PPI sectors in the wind farm.*

Figure 3.4 shows the top view of the scattered measurement points within the chosen altitude range of the PPI scans of each LIDAR. Figure 3.5 next to it illustrates the position of these PPI scans with respect to the »alpha ventus« wind farm layout. The LIDARs are distinguished by color and the names are indicated. The parameters characterizing the scanning scenario are listed in Table 3.6. Since the LIDARs both scan a relatively small azimuth range of 40 or 50 deg, they can cover the scan area more than once within the 10 minute time frames. WLS2 and WLS3 perform 7 and 5 sweeps per 10 minutes, respectively.

Table 3.6: *LIDAR scan parameters of cases 21-24.*

	WLS2	WLS3
χ [deg]	270-310	130-180
δ [deg]	2	2.8
r [m]	1400-2200	1100-1800
Number of scans	7	5

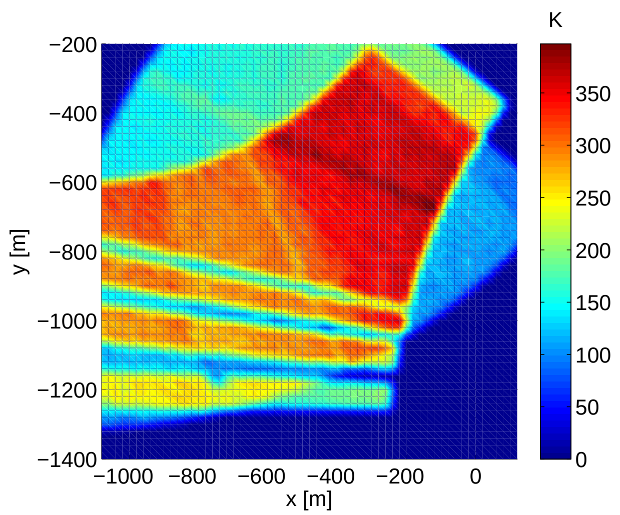

Figure 3.6: *Number of measurements K used per grid point p.*

Figure 3.6 shows the number of measurements considered for the MuLiWEA main matrix equation (Section 2.1) per grid point. A grid resolution of 20 m is used for the wind fields and the radius of influence *R* is determined to be 20 m as well. This means that the circles with radius of influence for neighboring grid points overlap and therefore some data is used more than once in the system. It can be seen that the LIDAR WLS2 has a few small blind spots in the south region of the scan. Because of the radially distributed measurements, the measurement density is not homogeneous and varies between 100 and 350 points per grid point. The reason for the relatively large *R* is the attempt to include enough measurement data at all grid points. The value was found through an iterative method of trial and error. Note that the plots for the scattered measurement points and the number of measurement points are highly similar for each time interval. These examples are representative for the duration of the scenario.

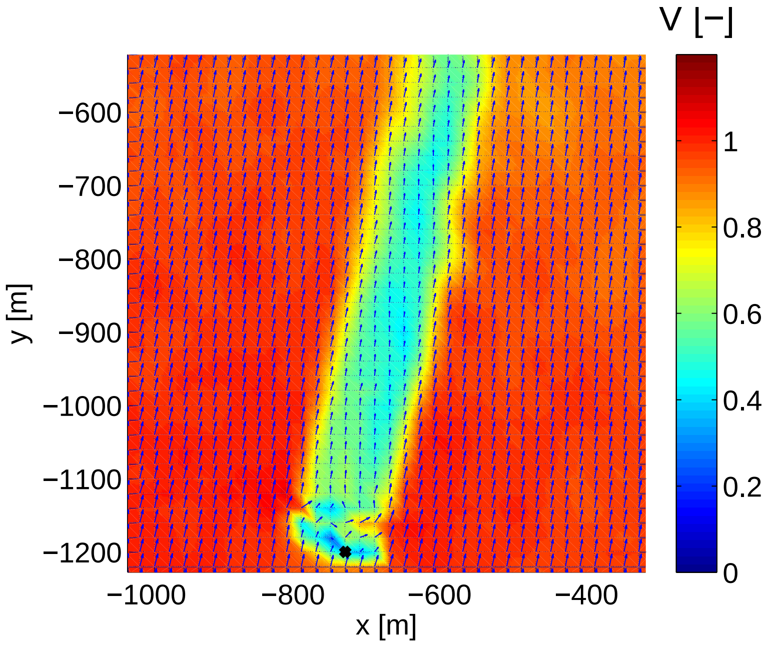

Figure 3.7: *Example 2D wind field plot, normalized to the ambient wind speed at hub height.*

An example of an evaluated 2D wind field is plotted in Figure 3.7. It contains the wake of time interval 8 (see Table 3.5). The 2D wind field is displayed as a color plot of the absolute wind speed, with an arrow plot on top of this showing the wind direction. The wind speed component perpendicular to the main wind direction is relatively small. For the further wake analysis, only the absolute wind speed in the wake direction is considered.

3.2.3 Comparison of Wake Profiles

In Figures 3.8-3.22, the evaluated wind fields for the considered time intervals are plotted. The start of the time interval is indicated above the plot. The number of the interval corresponds to the list in Table 3.5. In all figures, the position of AV10 is indicated with a black dot. The wake centerline deficit and lateral profiles are indicated with black lines at the positions ($1D$: $0.5D$: $5D$) downstream of the turbine. The width of the lateral lines is $2D$. The method used to locate and extract the wake position is explained in Appendix B. The absolute wind speed V is normalized with the ambient wind speed at hub height measured at FINO1, see Table 3.5. With this dimensionless wind speed, it is easier to directly compare the wakes at different time intervals with each other.

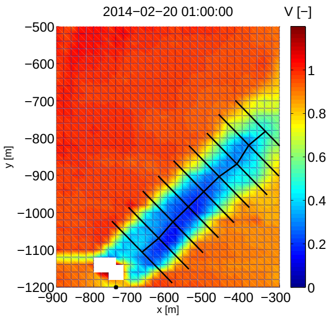

Figure 3.8: *Wind field of interval 1.*

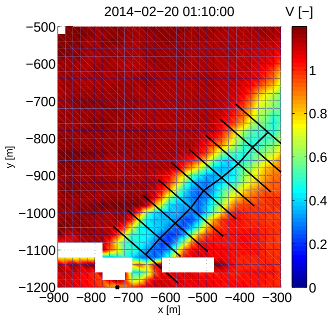

Figure 3.9: *Wind field of interval 2.*

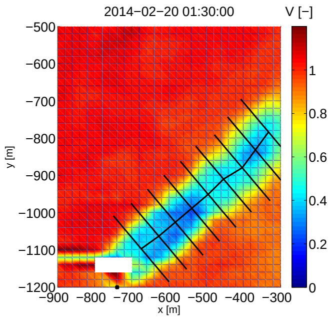

Figure 3.10: *Wind field of interval 3.*

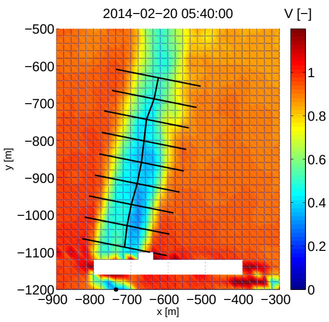

Figure 3.11: *Wind field of interval 4.*

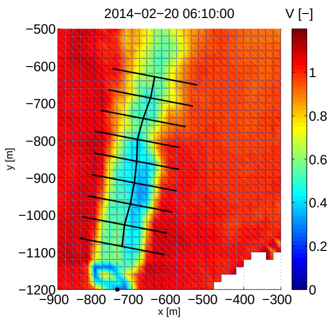

Figure 3.12: *Wind field of interval 5.*

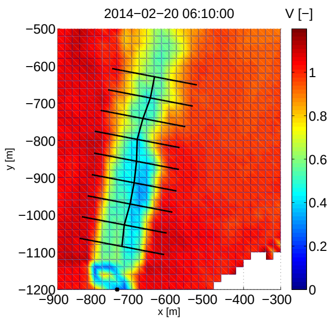

Figure 3.13: *Wind field of interval 6.*

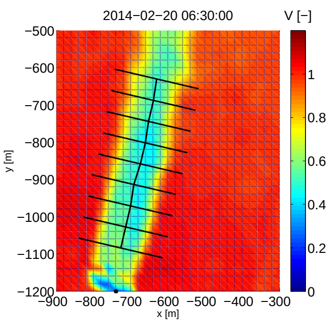

Figure 3.14: *Wind field of interval 7.*

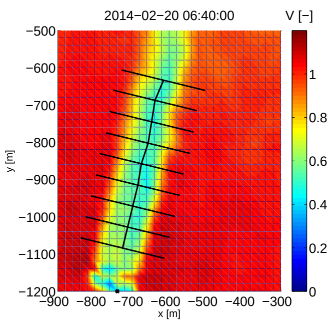

Figure 3.15: *Wind field of interval 8.*

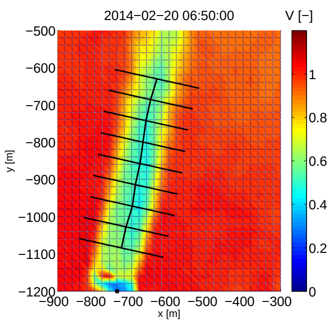

Figure 3.16: *Wind field of interval 9.*

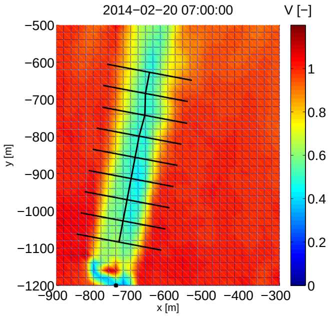

Figure 3.17: *Wind field of interval 10.*

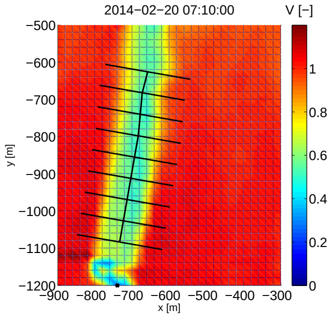

Figure 3.18: *Wind field of interval 11.*

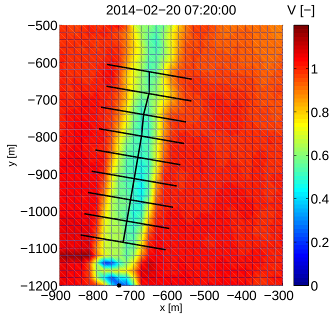

Figure 3.19: *Wind field of interval 12.*

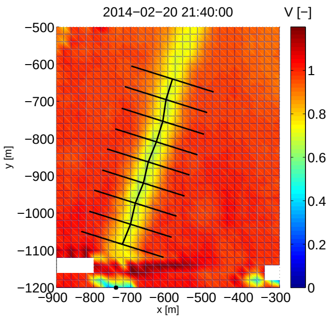

Figure 3.20: *Wind field of interval 13.*

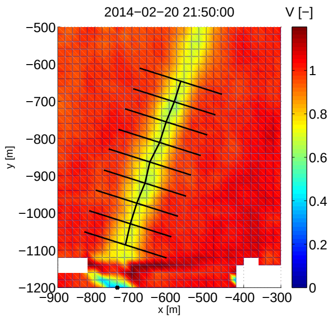

Figure 3.21: *Wind field of interval 14.*

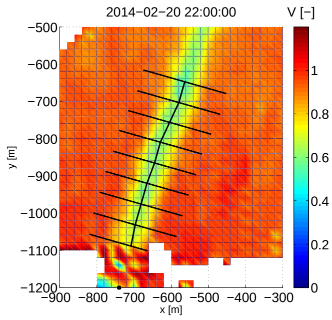

Figure 3.22: *Wind field of interval 15.*

By carefully studying the figures, the following general remarks can be made:

- The blind spots of WLS2, seen as a lack of measurements in Figure 3.6, result in some data gaps at the south side of the wind fields and just north of the wind turbine AV10.
- During several time intervals, the wake does not maintain the same direction throughout its length. Especially during time intervals 4, 10, 11 and 12 a slight deflection to the left can be noticed. During time intervals 5 and 6, there is a deflection to the right. The wake deflections do not seem to be correlated with the marginal offset between the inflow direction and the yaw of AV10. Possibly the wake direction could be influenced by the wind flow through the wind farm and presence of other wind turbines.
- The wakes are not always radially symmetric. Especially during time intervals 4, 5 and 6, deviations occur.
- During the time intervals 13, 14 and 15, the wake has a significantly smaller width compared to the other intervals. This is an effect of the relatively high ambient wind speed and thus a relatively low C_T value (see Figure 3.3). Also the velocity deficit is relatively small for the same reason.

In Figures 3.23-3.37, the extracted wake profiles for the fifteen time intervals are plotted. The profiles are shown for positions $(2D : 0.5D : 5D)$ downstream of the turbine. Namely, the FLaP model only predicts the far wake (>=2D). The extracted wake profiles are shown in black and the wake profiles simulated by FLaP are shown in red. The wind speed is normalized with the FINO1 measured wind speed and the x- and y-coordinates are normalized to the wind turbine diameter D.

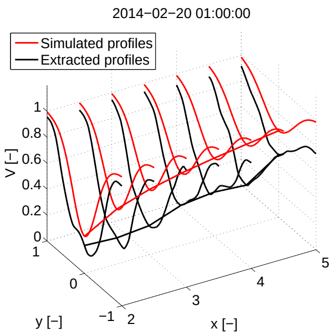

Figure 3.23: *Wake profiles of interval 1.*

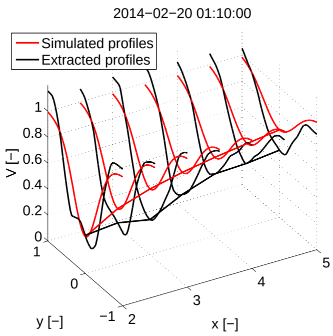

Figure 3.24: *Wake profiles of interval 2.*

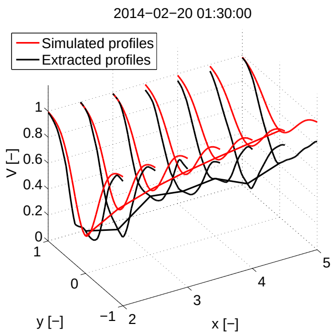

Figure 3.25: *Wake profiles of interval 3.*

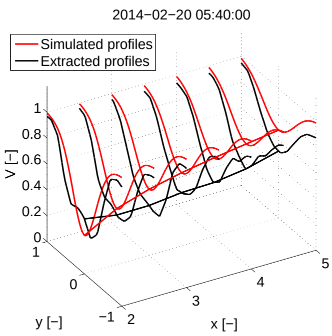

Figure 3.26: *Wake profiles of interval 4.*

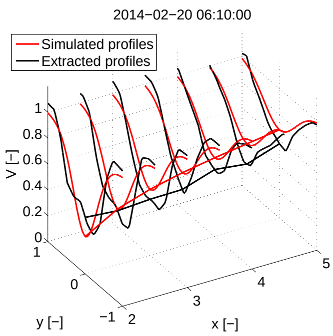

Figure 3.27: *Wake profiles of interval 5.*

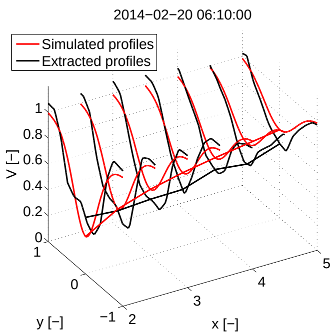

Figure 3.28: *Wake profiles of interval 6.*

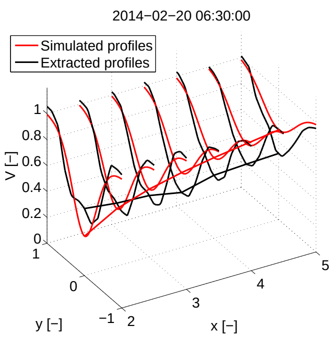

Figure 3.29: *Wake profiles of interval 7.*

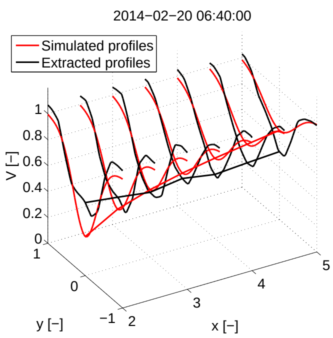

Figure 3.30: *Wake profiles of interval 8.*

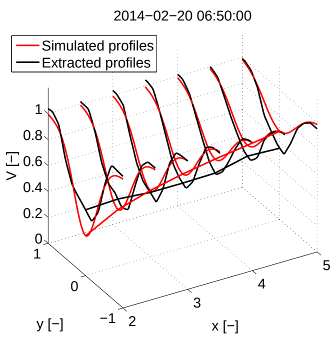

Figure 3.31: *Wake profiles of interval 9.*

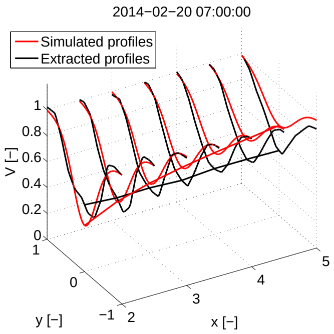

Figure 3.32: *Wake profiles of interval 10.*

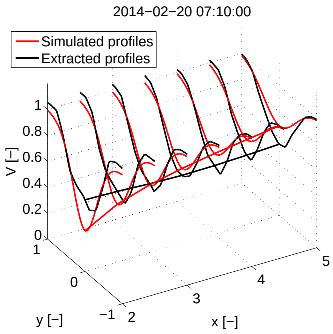

Figure 3.33: *Wake profiles of interval 11.*

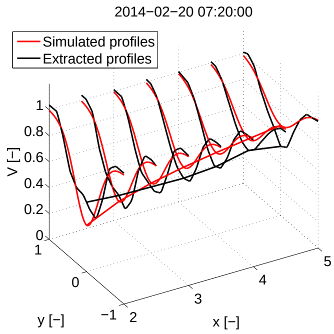

Figure 3.34: *Wake profiles of interval 12.*

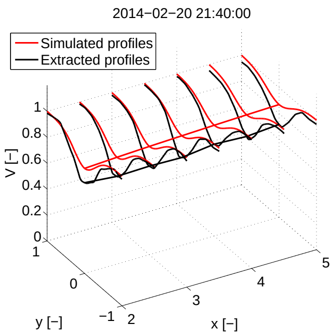

Figure 3.35: *Wake profiles of interval 13.*

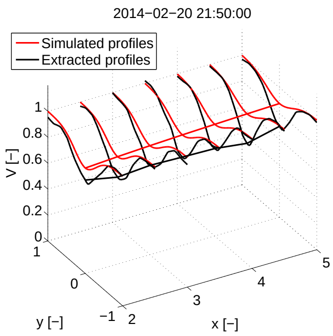

Figure 3.36: *Wake profiles of interval 14.*

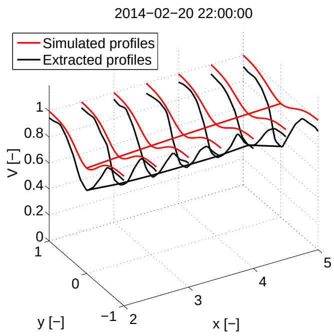

Figure 3.37: *Wake profiles of interval 15.*

By studying the wake profile plots, the following remarks can be established:

- For most cases, the simulated wake profiles indicate a quicker wake recovery than measured; in general higher wind speeds are predicted by the wake model. This could be caused by inaccuracies on the input parameters of the wake model or other relevant effects that are not included in the wake model.

- For most cases, the evaluated wake profiles in the first part of the wake have a different shape than the simulated ones. In fact, the FLaP model assumes a Gaussian shape for the wake profiles, whereas here a *double* Gaussian would be a better representation. Figure 3.38 shows a comparison between a single and a double Gaussian profile. In the evaluated cases, a shape similar to the latter can be observed within a downstream distance of approximately $3D$ behind the wind turbine. The shape is a result of the induction factor distribution over the wind turbine rotor. Most of the energy is extracted from the wind at the middle sections of a blade. The wind turbine hub and the blade roots do not contribute a lot to the generated power and therefore the velocity deficit is smaller directly behind the hub. Therefore this effect is visible in the centerline deficit. The minimum wind speed in the profile does not coincide with the center of the profile.

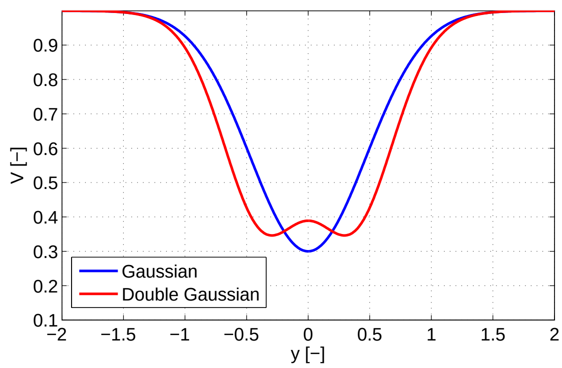

Figure 3.38: *Comparison of a Gaussian and double Gaussian wake profile.*

From the wake profiles in Figures 3.23-3.37, the two most relevant parameters that can be extracted are the wake width W_w and the centerline wake deficit W_d. The wake width is defined as the 2σ parameter of a Gaussian distribution fit through the wake profile. This parameter is normalized to the turbine diameter. The velocity deficit is the difference between the ambient wind speed and the local wake wind speed, normalized to the ambient wind speed itself. Working with dimensionless parameters allows for a better comparison between different measurement sets.

The fifteen time intervals as seen in Table 3.5 can be grouped into three sets which have highly similar atmospheric conditions. They are listed in Table 3.7:

Table 3.7: *Conditions of the three wake sets.*

Set	Time intervals	Stability	V [m/s]
1	1-3	Neutral	10
2	4-12	Near unstable	11
3	13-15	Near stable	16

From the wake profiles shown before in the 3D view, the parameters W_w and W_d are extracted and plotted in Figures 3.39-3.44 for the three established wake sets. These 2D plots are a more convenient way to visualize said parameters and analyze them separately. For all three cases, the measurements of the W_w and W_d parameters are scattered and a mean trend is plotted through. This is done for both the evaluated wake and the simulated wake. Also the mean accuracy bounds are shown for the velocity deficit, as calculated in the error analysis (Section 2.2). The accuracy of the wake width plot is related to the wind field resolution of 20 m. This is represented by the resolution bounds around the mean evaluated wake width. This is a conservative estimate, while the Gaussian fit will probably cause an error which is significantly smaller than this resolution.

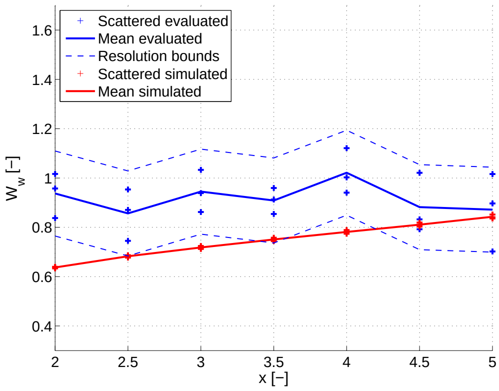

Figure 3.39: *Wake width for intervals 1-3.*

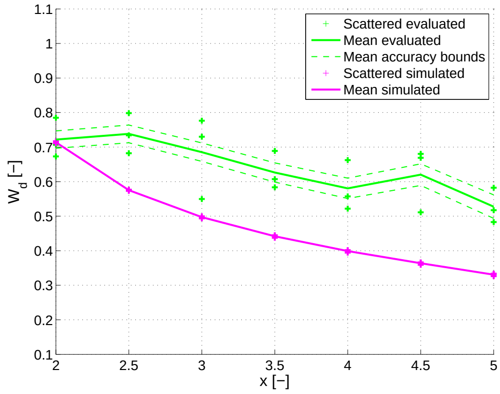

Figure 3.40: *Wake deficit for intervals 1-3.*

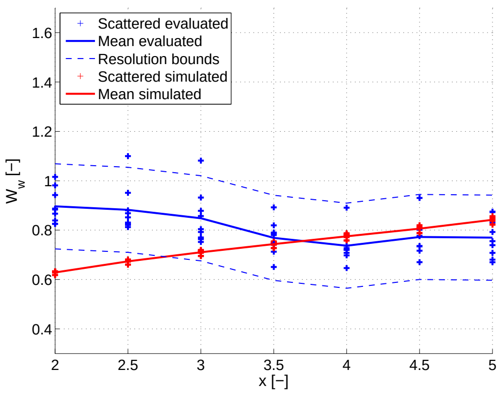

Figure 3.41: *Wake width for intervals 4-12.*

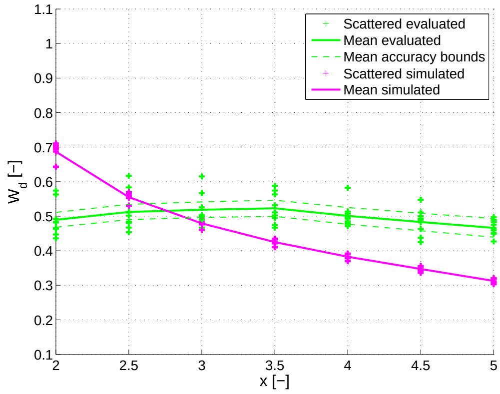

Figure 3.42: *Wake deficit for intervals 4-12.*

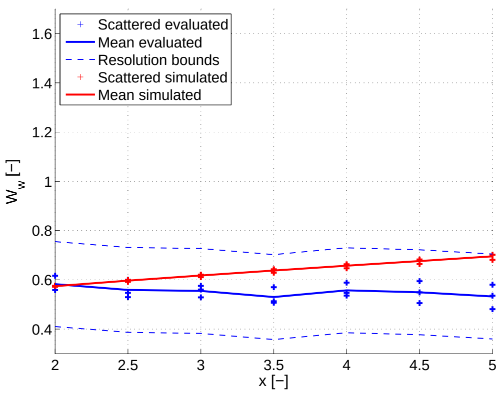

Figure 3.43: *Wake width for intervals 13-15.*

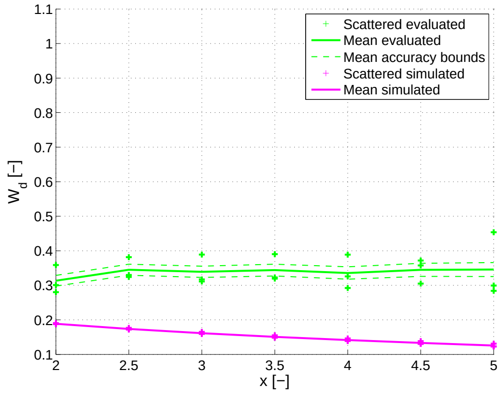

Figure 3.44: *Wake deficit for intervals 13-15.*

The following observations can be made based on the figures:

- The wake expansion predicted by the FLaP wake model does not resemble the measurements well. For the intervals 1-3, the evaluated wake width fluctuates around 0.9 turbine diameters. For the largest part, the simulation underestimates the width with about 0.2. For the intervals 4-12 but also 13-15, the measured wake is contracting instead of expanding. Possibly the far wake is influenced by the flow around wind turbines AV7 and AV8, which are located to the north of AV10 (see Figure 3.1). The presence of other turbines is not modeled by FLaP. Note that there is a significantly high inaccuracy because of the used resolution. The major part of the simulated wake width lies inside of the resolution bounds of the evaluated wake width.

- The evaluated wake velocity deficit does not show such a quick wake recovery as the simulation predicts. For the distances below $3D$, the wake deficit evaluated from the measurements is expected to be smaller than the model, because of the difference between the single and double Gaussian profiles as explained before. However, in general the wake deficit is underestimated with 0.1-0.2 by the model.

- As expected from the higher wind speeds and thus lower C_T values of the turbine (see Figure 3.3), intervals 13-15 show a significantly smaller wake width of about 0.5-0.6 and a smaller wake centerline deficit of 0.3-0.4.

- Unfortunately, there is not enough data available to make statements about the isolated effect of e.g. atmospheric stability on the wake width and deficit. To do this, more time intervals should be evaluated to be able to cover a wider range of different wind speeds and atmospheric conditions and thus provide statistics.

Note that the FLaP wake model was applied without considering the effect of other turbines. Also the Gaussian shape of the initial wake profile is a simplification of the actual shape. On top of this, it is not known what the uncertainties are for the wake model inputs and how this affects the end result.

4 Conclusion and Future Research Recommendations

The conclusion is separated into two parts. Section 4.1 will evaluate the performance of the MuLiWEA algorithm and the limitations on its application. Section 4.2 analyzes the evaluation of the wakes and the comparison to models. In both two sections, recommendations are made for carrying out further research on the combined topic of using LIDAR systems to characterize wakes in an offshore wind farm.

4.1 Conclusion on MuLiWEA

In Section 2.2 on the error analysis of MuLiWEA, the general structure of the numerical error was evaluated. The main conclusion of this analysis is that the numerical error has a large magnification in the vicinity of the line-of-sight that is shared by two LIDARs, i.e. the line with $\Delta\chi = 180°$. In general, the error is mainly dependent on the accuracy with which the used LIDAR scanner can measure the v_{LOS}. It has to be noted the analysis was done on an equation system similar to MuLiWEA, so there might still be some numerical error propagation effects of MuLiWEA that are not predicted by the used error analysis model.

In Section 2.3, the MuLiWEA was validated. It concludes that the algorithm performs with sufficient accuracy in case of an optimal LIDAR setup. The non-optimal LIDAR setup with a $\Delta\chi = 180°$ does not provide any useful results due to the intrinsically high errors, as predicted before by the error analysis. Although the mean average error for the absolute wind speed field, the wind direction field and the wake profiles is sufficiently low, some local significant errors were observed. These errors are likely caused by the heterogeneous measurement point distribution over the grid that has some local scarcities of data, which correspond to the local relatively high errors. Also part of the MuLiWEA numerical error propagation that has not been modeled could play a part in magnifying these errors.

The best accuracy of an evaluated wind field is reached when evaluating a plane at hub height. In this case, all the measurements within the selected altitude range are guaranteed to lie inside the wake. Also the wake is radially symmetric around this altitude. Especially when evaluating the wake at the upper blade tip height, mixing of measurements from inside and outside the wake combined with the wake asymmetry at this height will cause a lower accuracy of the evaluated wind field.

The continuity adjustment part of MuLiWEA significantly improves the accuracy of the evaluated wind fields. Especially in case of local data gaps or scarce data, the ill-defined matrix equation is improved by adding the extra lines of the continuity equation to the system. Unfortunately, the error analysis in Section 2.2 does not model the general quantitative improvement of the wind fields as a result of the continuity adjustment implementation.

Rough estimates of the optimal altitude selection parameter C_h and the radius of influence R are yielded in an attempt to optimize the MAE. The dimensionless C_h should be in the order of 0.3-0.4 for an accurate wind field evaluation and the optimal radius of influence R is highly dependent on the measurement density and the accuracy of the used LIDAR system. It is hard to generalize the results of the validation for the parameter R, because no errors were modeled on the LIDAR measurements. In a real wind field, these errors cause the need of more measurements per grid point thus a larger R to average out the effect and increase the accuracy.

The following recommendations are made for future research:

- Multiple-LIDAR setups have to be chosen carefully, such that two LIDARs are never measuring in an identical line-of-sight, i.e. the line with $\Delta\chi = 180°$. An optimal setup is able to scan an area within close range (< 2 km) and a relative azimuth angle between two LIDARs of $\Delta\chi = 90°$.

- The LIDAR scans have to be planned in such a way that the major part of the measurements are taken in a reasonable altitude range centered around hub height. The ideal altitude range has been determined as $[hh - C_h D/2, hh + C_h D/2]$ with a C_h of around 0.3-0.4.

- A more thorough numerical error analysis needs to be performed on the specific linear system of the MuLiWEA, to make a quantification of the effects of its sub-elements on the wind field error.

- The consequence of neglecting the vertical component of the wind speed has to be investigated more thoroughly, in terms of the error imposed on the absolute horizontal wind speed. Another option is including this component in the analysis. To do this, at least three LIDARs are needed, of which one should measure with relatively high elevation angles to cover a sufficient component of the vertical wind speed for numerical computation.

- The filter function that is used in the MUSCAT [6] could be implemented in MuLiWEA to assess its effect. This way, the assumption that the filter is not applicable in case of measuring large velocity gradients which occur in wakes, can be verified.

4.2 Conclusion on the Wake Evaluation

In Section 3.2, one scenario was used to evaluate wakes and compare them to the FLaP wake model. It is concluded that this wake model is not able to accurately predict all characteristics of the wake that can be observed from the measurements. Also, not enough data was available to statistically analyze the effect of atmospheric conditions.

The following recommendations are made for future research:

- It would be interesting to use and evaluate more sophisticated wake models, which are able to predict the wind flow through a wind farm and thus accounts for interaction between wakes. In this master thesis, MuLiWEA was applied on a single wake. To better understand the behavior of wakes in wind farms, the algorithm needs to be applied to a larger part of the wind farm to evaluate multiple wakes. The more sophisticated wake models will be required to validate these evaluated wind fields.
- In order to make a statistical analysis on the wake characteristics and the parameters that influence them, a specific well-planned scanning scenario has to be performed for a significantly long time, preferably a year to include seasonal weather effects, but at least for a few weeks. This way, there is a sufficient variety in atmospheric and wind turbine conditions, such that the influence of each relevant parameter on the wake can be studied separately. The area of the scan has to be sufficiently large as to capture the wake in case of different occurring wind directions.

Bibliography

[1] JCGM - Evaluation of Measurement Data: Guide to the Expression of Uncertainty in Measurement, 2008.

[2] J.F. Ainslie. Calculating the Flowfield in the Wake of Wind Turbines. *Journal of Wind Engineering and Industrial Aerodynamics*, 27:213–224, 1988.

[3] R.J. Barthelmie, K. Hansen, S.T. Frandsen, O. Rathmann, J.G. Schepers, W. Schlez, J. Phillips, K. Rados, A. Zervos, E.S. Politis, and P.K. Chaviaropoulos. Modelling and Measuring Flow and Wind Turbine Wakes in Large Wind Farms Offshore. *Wiley Interscience Wind Energy*, 12:431–444, 2009.

[4] C. Bartsch. Fact Sheet »alpha ventus«. Technical report, Deutsche Offshore-Testfeld und Infrastructur GmbH & Co. KG, 2012.

[5] O. Bousquet. *Doppler Radar Observations - Weather Radar, Wind Profiler, Ionospheric Radar, and Other Advanced Applications*, chapter 8, pages 205–230. InTech, 2012.

[6] O. Bousquet and M. Chong. A Multiple-Doppler Synthesis and Continuity Adjustment Technique (MUSCAT) to Recover Wind Components from Doppler Radar Measurements. *Journal of Atmospheric and Oceanic Technology*, 15:343–359, 1998.

[7] T. Burton, N. Jenkins, D. Sharpe, and E. Bossanyi. *Wind Energy Handbook*, chapter 2, pages 33–36. Wiley & Sons, 2011.

[8] M. Chong and C. Campos. Extended Overdetermined Dual-Doppler Formalism in Synthesizing Airborne Doppler Radar Data. *Journal of Atmospheric and Oceanic Technology*, 13:581–597, 1996.

[9] G. P. Cressman. An Operational Objective Analysis System. *Monthly Weather Review*, 87 (10):367–374, 1959.

[10] S. Drechsel, M. Chong, G. J. Mayr, M. Weissmann, R. Calhoun, and A. Dörnbrack. Three-Dimensional Wind Retrieval: Application of MUSCAT to Dual-Doppler Lidar. *Journal of Atmospheric and Oceanic Technology*, 26:635–646, 2009.

[11] S. Frandsen, R. Barthelmie, S. Pryor, O. Rathmann, S. Larsen, and J. Højstrup. Analytical Modelling of Wind Speed Deficit in Large Offshore Wind Farms. *Wind Energy*, 9:39–53, 2006.

[12] F. González-Longatt, P. Wall, and V. Terzija. Wake Effect in Wind Farm Performance: Steady-state and Dynamic Behavior. *Renewable Energy*, 39:329–338, 2012.

[13] K. Hansen, R. Barthelmie, S. Ott, and G. C. Larsen. Park Power Deficit due to Atmospheric Stability. In *The Science of Making Torque from Wind 2012 (TORQUE 2012)*, 2012.

[14] B. D. Hirth and J. L. Schroeder. Documenting Wind Speed and Power Deficits behind a Utility-Scale Wind Turbine. *Journal of Applied Meteorology and Climatology*, 52:39–46, 2012.

[15] G. V. Iungo, Y. Wu, and F. Porté-Agel. Field Measurements of Wind Turbine Wakes with Lidars. *Journal of Atmospheric and Oceanic Technology*, 30:274–287, 2012.

[16] N. O. Jensen. A Note on Wind Generator Interaction. Technical report, Risø National Laboratory of Denmark, 1983. RISØ-M-2411.

[17] J. Jonkman, S. Butterfield, W. Musial, and G. Scott. Definition of a 5-MW Reference Wind Turbine for Offshore System Development. Technical Report TP-500-38060, NREL - National Renewable Energy Laboratory, 2009.

[18] P. K. Kundu and I. M. Cohen. *Fluid Mechanics*. Elsevier Academic Press, 2008.

[19] B. Lange, H. P. Waldl, A. G. Guerrero, D. Heinemann, and R. J. Barthelmie. Modelling of Offshore Wind Turbine Wakes with the Wind Farm Program FLaP. *Wind Energy*, 6:87–104, 2003.

[20] T. Neumann, K. Nolopp, V. Riedel, M. Strack, K. Herklotz, and J. Stein. Assessment of One Year Wind Measurements on the First Offshore Wind Research Platform in the German Bight - FINO1. In *DEWEK 2004*, 2004.

[21] N. G. Nygaard. Wakes in Very Large Wind Farms and the Effect of Neighbouring Wind Farms. In *Torque Conference 2014 Copenhagen*, 2014.

[22] S. Raasch and M. Schröter. PALM - A Large-Eddy Simulation Model Performing on Massively Parallel Computers. *Meteorologische Zeitschrift*, 10:363–372, 2001.

[23] D. Trabucchi. Wind Physics Measurement Project - Lecture Slides on LIDAR Measurements. Technical report, ForWind, Carl von Ossietzky Universität Oldenburg, 2013.

[24] C. Weitkamp. *Range Resolved Optical Remote Sensing of the Atmoshpere*, chapter 12, pages 325–353. Springer, 2005.

A Weighting Functions for Grid Interpolation

As explained before, in the interpolation of the LIDAR measurement data on the desired grid, two weighting functions are needed. One weighs based on the distance from the grid point with a Cressman weighting function (w_f) [9] and the other is a weight per LIDAR (w_L). The two weights can be multiplied with each other to form the combined weight $w = w_f w_L$.

As stated before, the Cressman weight is assigned as a function on the distance. Around each grid point, a circle with radius of influence R is drawn. Measurements with a distance r away from the grid point, get a weight according to the formula:

$$w_f = \frac{R^2 - r^2}{R^2 + r^2} \tag{A.1}$$

The weight has a value of 1 for measurements exactly at the grid point, and equals zero at or outside the boundary R. Plots of the Cressman weighting function can be observed in Figures A.1 and A.2.

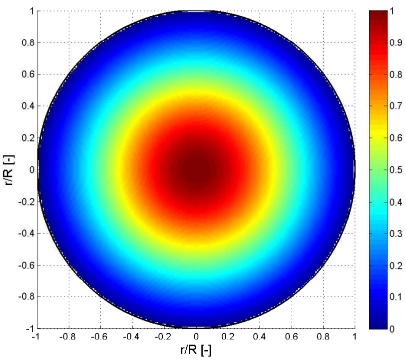

Figure A.1: *Cressman weighting function, top view.*

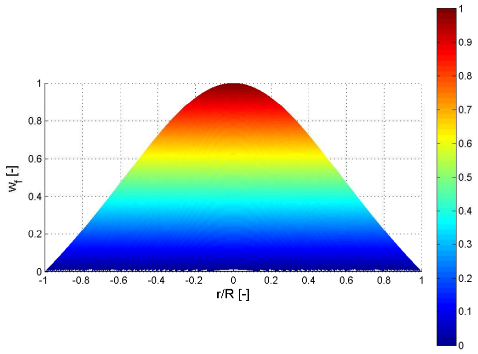

Figure A.2: *Cressman weighting function, side view.*

Since the measurements from multiple LIDARs are not evenly distributed, it is important to make sure that each LIDAR contributes to the evaluated grid point to the same extent.

First, a vector is made containing the measurements per LIDAR within the circle of influence around a grid point. Then, the weight per LIDAR w_L is assigned as:

$$w_L = \frac{1}{K_L} \frac{K}{L} \tag{A.2}$$

In this equation, K is the total amount of measurements considered for the grid point, K_L is the number of measurements per specific LIDAR for the grid point and L is the amount of LIDARS which contribute to the grid point. This number can be 1,2 or 3. Each LIDAR gets a unique weight w_L for a specific grid point, but this weight is applied to all the associated measurement points such that $\sum_{k=1}^{K} w_{L_k} = K$.

So in the overall linear system, grid points with more measurements available in the circle of influence still get a higher importance.

B Wake Extracting Algorithm

In order to characterize wakes, an algorithm is written that attempts to find the wake based on a known turbine position and wind direction. With these two function inputs, it defines lines with length $2D$ (D is the wind turbine diameter) orthogonal to the wind direction, at a range of distances ($1D : 0.5D : 5D$) downstream of the turbine. It is actually an iterative process, consisting of the following steps:

1. The turbine position and the wind direction from the FINO1 data are used to predict the center line of the wake downstream of the turbine.
2. Wake profiles are extracted perpendicular to the predicted wake direction.
3. The center of each of these lateral wake profiles is found by fitting a Gaussian curve through the profile. The offset between these centers and the estimated center line is calculated.
4. A line is fitted through these centers and the angle between this line and the initially assumed center line is defined.
5. The wake direction is updated with this correction angle and the wake profiles are calculated again.

There are a few possible reasons why the direction of the wake needs to be updated, i.e. why the direction of the wake can differ from the FINO1 measured wind direction at hub height:

- The atmospheric wind direction may vary locally.
- The turbine may have a yaw misalignment, such that the wake direction deviates from the inflow wind direction.
- Blockage of the wind vane on the FINO1 mast can occur if the wind is coming from specific directions. This may cause the wind vane to give an incorrect reading.
- The wind direction at FINO1 may be different than the ambient wind direction due to influence by the wind farm.

For case 21 of the catalog (Appendix D), the evaluated wind field of the wake of turbine AV10 is plotted in Figure B.1 and additionally the extracted wake is shown separately in Figure B.2. An arbitrary time domain of 10 minutes is selected. The wake is extracted along the center line predicted by the FINO1 wind direction. In this specific case, the FINO1 wind direction deviates from the actual wake direction. This can be seen as a misaligned wake track in Figure B.1 and misalignment between the centers of the Gaussian profiles and the wake profile centers in Figure B.2. If the wind direction is updated according to the steps mentioned earlier, the extraction of the wake has the correct direction. This is illustrated by Figures B.3 and B.4.

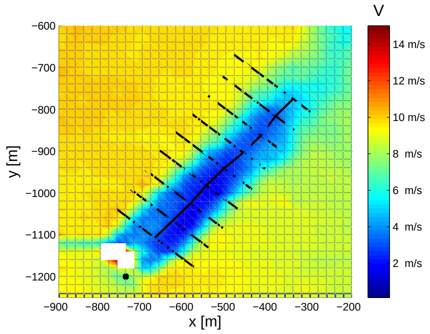

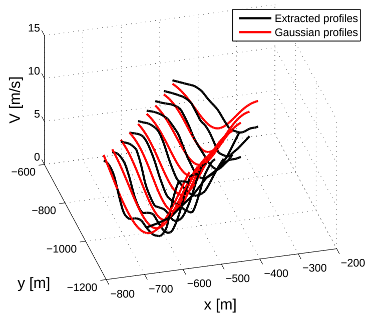

Figure B.1: *Wind field with misaligned wake extraction direction.*

Figure B.2: *Extracted wake profiles with misaligned centers.*

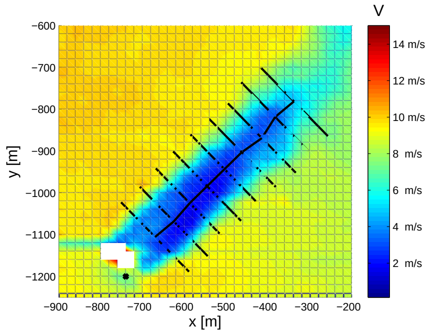

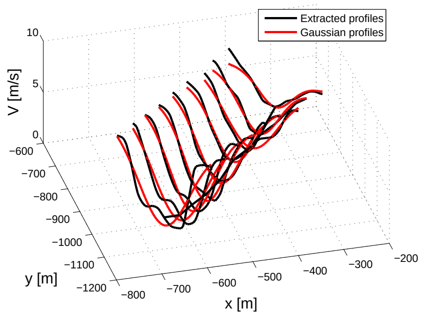

Figure B.3: *Wind field with corrected wake extraction direction.*

Figure B.4: *Extracted wake profiles with corrected centers.*

C Partial Derivatives for the Error Analysis

Here is an overview of the twelve relevant partial derivatives for the determination of the error on wind fields evaluated by Dual-LIDAR, as presented in Section 2.2. First the expressions for the wind speeds u and v are repeated:

$$u = \frac{N_u}{D_u} = \frac{\cos(\chi_{C_1})\cos(\delta_1)v_{LOS_2} - \cos(\chi_{C_2})\cos(\delta_2)v_{LOS_1}}{\cos(\chi_{C_1})\cos(\delta_1)\sin(\chi_{C_2})\cos(\delta_2) - \sin(\chi_{C_1})\cos(\delta_1)\cos(\chi_{C_2})\cos(\delta_2)} \tag{C.1}$$

$$v = \frac{N_v}{D_v} = \frac{\sin(\chi_{C_1})\cos(\delta_1)v_{LOS_2} - \sin(\chi_{C_2})\cos(\delta_2)v_{LOS_1}}{\sin(\chi_{C_1})\cos(\delta_1)\cos(\chi_{C_2})\cos(\delta_2) - \cos(\chi_{C_1})\cos(\delta_1)\sin(\chi_{C_2})\cos(\delta_2)} \tag{C.2}$$

The wind speeds u and v are defined with their numerator and denominator, respectively N_u, N_v and D_u, D_v. These terms will be used in the expression for the partial derivatives in order to keep the notation concise.

$$\frac{\partial u}{\partial v_{LOS_1}} = \frac{-\cos(\chi_{C_2})\cos(\delta_2)}{D_u} \tag{C.3}$$

$$\frac{\partial u}{\partial v_{LOS_2}} = \frac{\cos(\chi_{C_1})\cos(\delta_1)}{D_u} \tag{C.4}$$

$$\begin{aligned}\frac{\partial u}{\partial \chi_{C_1}} &= \frac{1}{D_u^2}\Big[D_u\Big(-\sin(\chi_{C_1})\cos(\delta_1)v_{LOS_2}\Big)\\ &-N_u\Big(-\sin(\chi_{C_1})\cos(\delta_1)\sin(\chi_{C_2})\cos(\delta_2) - \cos(\chi_{C_1})\cos(\delta_1)\cos(\chi_{C_2})\cos(\delta_2)\Big)\Big]\end{aligned} \tag{C.5}$$

$$\begin{aligned}\frac{\partial u}{\partial \chi_{C_2}} &= \frac{1}{D_u^2}\Big[D_u\Big(\sin(\chi_{C_2})\cos(\delta_2)v_{LOS_1}\Big)\\ &-N_u\Big(\cos(\chi_{C_1})\cos(\delta_1)\cos(\chi_{C_2})\cos(\delta_2) + \sin(\chi_{C_1})\cos(\delta_1)\sin(\chi_{C_2})\cos(\delta_2)\Big)\Big]\end{aligned} \tag{C.6}$$

$$\begin{aligned}\frac{\partial u}{\partial \delta_1} &= \frac{1}{D_u^2}\Big[D_u\Big(-\cos(\chi_{C_1})\sin(\delta_1)v_{LOS_2}\Big)\\ &-N_u\Big(\cos(-\chi_{C_1})\sin(\delta_1)\sin(\chi_{C_2})\cos(\delta_2) + \sin(\chi_{C_1})\sin(\delta_1)\cos(\chi_{C_2})\cos(\delta_2)\Big)\Big]\end{aligned} \tag{C.7}$$

$$\begin{aligned}\frac{\partial u}{\partial \delta_2} &= \frac{1}{D_u^2}\Big[D_u\Big(\cos(\chi_{C_2})\sin(\delta_2)v_{LOS_1}\Big)\\ &-N_u\Big(-\cos(\chi_{C_1})\cos(\delta_1)\sin(\chi_{C_2})\sin(\delta_2) + \sin(\chi_{C_1})\cos(\delta_1)\cos(\chi_{C_2})\sin(\delta_2)\Big)\Big]\end{aligned} \tag{C.8}$$

$$\frac{\partial v}{\partial v_{LOS_1}} = \frac{-\sin(\chi_{C_2})\cos(\delta_2)}{D_v} \tag{C.9}$$

$$\frac{\partial v}{\partial v_{LOS_2}} = \frac{\sin(\chi_{C_1})\cos(\delta_1)}{D_v} \tag{C.10}$$

$$\begin{aligned}\frac{\partial v}{\partial \chi_{C_1}} &= \frac{1}{D_v^2}\Big[D_v\Big(\cos(\chi_{C_1})\cos(\delta_1)v_{LOS_2}\Big) \\ &-N_v\Big(\cos(\chi_{C_1})\cos(\delta_1)\cos(\chi_{C_2})\cos(\delta_2) + \sin(\chi_{C_1})\cos(\delta_1)\sin(\chi_{C_2})\cos(\delta_2)\Big)\Big]\end{aligned} \tag{C.11}$$

$$\begin{aligned}\frac{\partial v}{\partial \chi_{C_2}} &= \frac{1}{D_v^2}\Big[D_v\Big(-\cos(\chi_{C_2})\cos(\delta_2)v_{LOS_1}\Big) \\ &-N_v\Big(-\sin(\chi_{C_1})\cos(\delta_1)\sin(\chi_{C_2})\cos(\delta_2) - \cos(\chi_{C_1})\cos(\delta_1)\cos(\chi_{C_2})\cos(\delta_2)\Big)\Big]\end{aligned} \tag{C.12}$$

$$\begin{aligned}\frac{\partial v}{\partial \delta_1} &= \frac{1}{D_v^2}\Big[D_v\Big(-\sin(\chi_{C_1})\sin(\delta_1)v_{LOS_2}\Big) \\ &-N_v\Big(-\sin(\chi_{C_1})\sin(\delta_1)\cos(\chi_{C_2})\cos(\delta_2) + \cos(\chi_{C_1})\sin(\delta_1)\sin(\chi_{C_2})\cos(\delta_2)\Big)\Big]\end{aligned} \tag{C.13}$$

$$\begin{aligned}\frac{\partial v}{\partial \delta_2} &= \frac{1}{D_v^2}\Big[D_v\Big(\sin(\chi_{C_2})\sin(\delta_2)v_{LOS_1}\Big) \\ &-N_v\Big(-\sin(\chi_{C_1})\cos(\delta_1)\cos(\chi_{C_2})\sin(\delta_2) + \cos(\chi_{C_1})\cos(\delta_1)\sin(\chi_{C_2})\sin(\delta_2)\Big)\Big]\end{aligned} \tag{C.14}$$

D Measurement Data Catalog

Case	Scenario Name	Start/End	WD	Wakes	Altitude	LIDAR WLS	Quality	Notes
1	FARMWAKE04	2013-08-15 15 21	SW	9,12	Scatter	23	Good	
2	FARMWAKE04	2013-08-15 21 16 03	SW	9,12	Scatter	23	Good	
3	FARMWAKE04	2013-08-16 03 09	SW	9,12	Scatter	23	Good	
4	FARMWAKE08	2013-09-30 16 21	E	5	Scatter	23	Medium	
5	FARMWAKE08	2013-10-01 16 21	E	5	Scatter	23	Medium	
6	FARMWAKELLJ01	2013-11-20 12 18	S	6,9	Scatter	23	Medium	13:30-13:40, 13:50-14:00, 14:20-14:30
7	FARMWAKELLJ01	2013-11-20 18 21 00	SE	7	Scatter	23	Medium	21:10-21:20, 21:40-21:50, 22:30-22:40, 23:20-23:30
8								
9								
10								
11								
12								
13	AV04WakeDualDoppler01	2014-02-25 20 26 00	S	4	HH	12	Very bad	Sector WLS1 too small to capture wake
14	AV04WakeDualDoppler01	2014-02-26 00 09	SW	4	HH	12	Very bad	Sector WLS1 too small to capture wake
15	AV04WakeDualDoppler01	2014-02-26 09 18	S	4	HH	12	Bad	Sector WLS1 too small to capture wake
16	AV04WakeDualDoppler01	2014-02-26 18 27 03	SW	4	HH	12	Bad	Sector WLS1 too small to capture wake

Case	Scenario Name	Start/End	WD	Wakes	Altitude	LIDAR WLS	Quality	Notes
17	AV04WakeDualDoppler01	2014-02-27 03 10	SW	4	HH	12	Very bad	Sector WLS1 too small to capture wake
18	SINGLEWAKEAV03	2014-02-06 13 14	SW	3	Scatter	23	Very bad	CNR WLS3 too low
19	SINGLEWAKEAV03	2014-02-12 10 11	SW	3	Scatter	12	Very bad	CNR WLS1 too low
20	SINGLEWAKEAV12	2014-02-06 11 13	SW	12	Scatter	23	Medium	WLS2 measures too high
21	WAKEAV10andWAKEAV0301	2014-02-20 00 03	SW	10	HH	23	Good	
22	WAKEAV10andWAKEAV0301	2014-02-20 03 06	SW	10	HH	23	Good	
23	WAKEAV10andWAKEAV0301	2014-02-20 06 09	SW	10	HH	23	Good	
24	WAKEAV10andWAKEAV0301	2014-02-20 21 21 00	SW	10	HH	23	Good	
25	WAKEAV10andWAKEAV0301	2014-02-21 00 02	SW	10	HH	23	Good	
26	WAKEAV10andWAKEAV0301	2014-02-21 02 04	SW	10	HH	23	Good	
27	AV06WakeDualDoppler01	2014-03-06 12 18		6				Erroneous command script
28	AV07WakeDualDoppler01	2014-03-10 10 16	N	7	HH	12	Good	Sector WLS1 small but wake partially captured, stops at 14:30
29	AV07WakeDualDoppler01	2014-03-10 16 11 00		7				No data!
30								
31								
32								

Case	Scenario Name	Start/End	WD	Wakes	Altitude	LIDAR WLS	Quality	Notes
33	AV03WakeDualDoppler01	2014-03-10 18 11 00	NE	3	HH	123	Medium	Data gaps WLS1 and WLS3
34	AV03WakeDualDoppler01	2014-03-11 00 09	NE	3	HH	1	Very bad	
35	AV03WakeDualDoppler01	2014-03-11 09 18	NE	3	HH	23	Medium	Data gaps WLS3
36	AV03WakeDualDoppler02	2014-03-11 10 17	NE	3	HH	1	Very bad	
37	AV03WakeDualDoppler02	2014-03-11 17 12 00	NE	3	HH	23	Very bad	CNR too low, stops at 20:30
38	AV03WakeDualDoppler03	2014-03-13 15 14 00	NW	3	HH	23	Medium	Data gap, low wind speed, 18:20<
39	AV03WakeDualDoppler03	2014-03-14 00 09	N	3	HH	23	Bad	Data gap, low wind speed, <5:00
40	AV03WakeDualDoppler04	2014-03-14 15 15 00	W	3	HH	23	Bad	Wake falls in data gap
41	AV03WakeDualDoppler04	2014-03-15 00 06	NW	3	HH	23	Bad	Wake falls in data gap
42	AV03WakeDualDoppler04	2014-03-15 06 12	NW	3	HH	23	Bad	Wake falls in data gap
43	AV03WakeDualDoppler04	2014-03-15 12 18	W	3	HH	23	Bad	Wake falls in data gap
44	AV03WakeDualDoppler04	2014-03-15 18 16 00	W	3	HH	23	Bad	Wake falls in data gap
45	AV03WakeDualDoppler04	2014-03-16 00 06	NW	3	HH	23	Very bad	Wake falls in data gap
46	AV03WakeDualDoppler04	2014-03-16 06 12	W	3	HH	23	Very bad	Wake falls in data gap
47	AV03WakeDualDoppler04	2014-03-16 12 18	W	3	HH	23	Bad	Wake falls in data gap
48								

Case	Scenario Name	Start/End	WD	Wakes	Altitude	LIDAR WLS	Quality	Notes
49	AV03WakeDualDoppler05	2014-03-17 17 18 00	W	6	HH	23	Very bad	Large data gap
50	AV03WakeDualDoppler05	2014-03-18 00 05	W	6	HH	23	Very bad	Large data gap
51	AV03WakeDualDoppler05	2014-03-18 05 10	W	6	HH	23	Very bad	Large data gap
52	AV06WakeDualDoppler02	2014-03-18 12 18	W	6	HH	12	Medium	Artefacts of the course data coverage
53	AV06WakeDualDoppler02	2014-03-18 18 19 00	W	6	HH	12	Medium	Artefacts of the course data coverage
54	AV06WakeDualDoppler02	2014-03-19 00 09	W	6	HH	12	Medium	Artefacts of the course data coverage
55	RADARCMP01	2013-12-07 01 04	NW	6	Low (23) Scatter (123)	123	Bad	2:40-2:50, 3:30-3:40
56	RADARCMP01	2013-12-07 04 07	NW	6	Low (23) Scatter (123)	123	Bad	
57	RADARCMP01	2013-12-08 01 04	W	6,9	Low (23) Scatter (123)	123	Medium	1:30-1:50, 2:00<
58	RADARCMP01	2013-12-08 04 07	W	6,9	Low (23) Scatter (123)	123	Medium	
59	RADARCMP01	2014-03-17 09 14	W	5,6,7,8,9	Low	23	Good	Multiple wakes, very low to the sea surface
60	LONGRANGE01	2013-11-08 18 21	SE	6,9,10,11	Low (23) Scatter (123)	123	Good	
61	LONGRANGE01	2013-11-08 21 09 00	SE	6,9,10,11	Low (23) Scatter (123)	123	Good	
62	LONGRANGE01	2013-11-09 00 03	SE	8	Low (23) Scatter (123)	123	Medium	
61	LONGRANGE01	2013-11-09 03 06	SE	8	Low (23) Scatter (123)	123	Medium	
62	LONGRANGE01	2013-11-09 06 09	W	5,6	Low (23) Scatter (123)	123	Bad	

Hiermit versichere ich, dass ich diese Arbeit selbständig verfasst und keine anderen als die angegebenen Quellen und Hilfsmittel benutzt habe. Außerdem versichere ich, dass ich die allgemeinen Prinzipien wissenschaftlicher Arbeit und Veröffentlichung, wie sie in den Leitlinien guter wissenschaftlicher Praxis der Carl von Ossietzky Universität Oldenburg festgelegt sind, befolgt habe.

Unterschrift: